THE DYNAMICS OF VISCOUS DROPLETS NEAR MICRO-PATTERNED SOLID SURFACES IN CREEPING FLOW

A Thesis
Submitted to the Graduate Faculty
of the
North Dakota State University
of Agriculture and Applied Science

By

Kevin Michael Beussman

In Partial Fulfillment
for the Degree of
MASTER OF SCIENCE

Major Department:
Mechanical Engineering

May 2014

Fargo, North Dakota

North Dakota State University
Graduate School

Title

The Dynamics of Viscous Droplets Near Micro-Patterned Solid Surfaces in Creeping Flow

By

Kevin Michael Beussman

The Supervisory Committee certifies that this ***disquisition*** complies with North Dakota State University's regulations and meets the accepted standards for the degree of

MASTER OF SCIENCE

SUPERVISORY COMMITTEE:

Dr. Yechun Wang
Chair

Dr. Xiangfa Wu

Dr. Iskander Akhatov

Dr. Xuefeng Chu

Approved:

5/16/2014
Date

Dr. Alan Kallmeyer
Department Chair

ABSTRACT

The interaction between droplets and solid surfaces is of great importance in industrial applications, biochemical processes, and fundamental materials research on surface wettability. In this work, a three-dimensional spectral boundary element method has been employed to investigate the dynamics of a viscous droplet moving under gravity influence normal and parallel to a micro-patterned solid surface. The dynamics of the droplet moving perpendicular to the substrate are investigated under the influence of Bond number, droplet size, and topological features of the substrate. We find that the droplet dynamics can be controlled by varying Bond number, droplet size, and pattern height and width; however, the pattern length has little effect. For a droplet moving parallel to the surface, the Bond number and pattern projection direction greatly change the droplet dynamics. However, after moving past the pattern, the droplet position, velocity, and deformation return to that of a flat-plate solution.

ACKNOWLEDGMENTS

This work was supported by the National Science Foundation under Grant No. CBET-1032514. I would like to thank Dr. Yechun Wang for all of her help performing this research, writing papers, and general guidance through the Master's program. I would also like to thank Dr. Daniel Ewert for his mentoring, help writing papers and grant proposals, and inspiring me to study biomedical related areas. My graduate committee has also been helpful with general advice for my research, and it has been a pleasure working with everyone at NDSU.

TABLE OF CONTENTS

LIST OF FIGURES

CHAPTER 1. INTRODUCTION

1.1. Viscous droplet dynamics

Viscous droplets moving in an immiscible medium is a subject which has been studied intensively. As a droplet moves through a viscous medium or interacts with other objects, the interface deforms due to an unbalance of forces such as drag, gravity, inertia, and surface tension. Surface tension counteracts other forces and tries to keep the droplet spherical. If the other forces are large enough, they can overwhelm surface tension and the droplet will burst.

The understanding of viscous droplets in an immiscible viscous fluid is important in industrial applications, lab-on-a-chip devices, and other microfluidic applications [29]. The ability to accurately predict droplet dynamics is essential to fully understanding the underlying physics and optimize these processes. In lab-on-a-chip applications, droplets of various fluids are controlled by microfluidic devices to promote droplet mixing or isolation of specific droplets [1, 29, 30, 38]. The droplet motion is typically controlled by either optimizing the geometry or by using electric fields [18, 30, 39]. The former has advantages over the latter by not having to worry about how the electric fields might adversely interact with the droplets (or cells in some cases).

Much of the theory behind viscous droplets comes originally from Taylor who discussed the viscosity of fluid emulsions and studied fluid interfaces [32, 33]. Taylor and Acrivos then studied the deformation of viscous droplets falling at terminal velocity at low Reynolds numbers [34]. Their work helped us understand the governing dynamics of viscous droplets moving in a viscous medium. Dandy *et al.* studied the buoyancy-driven motion for bubbles or droplets traveling through a quiescent liquid at moderate Reynolds numbers [3].

Recently, simulations have been performed on droplets falling in a channel filled with low-viscosity fluid using a finite element method [11] and high-viscosity fluid using a level

set method [22].

1.2. Droplet-substrate interaction

The interaction of a viscous droplet with a solid surface has been the focus of much research for applications in coatings, weathering, and microfluidics, to name a few. There are also possible applications in cell culturing. When culturing, cells are suspended in a solution before settling towards a substrate. The interaction of the cells with the substrate may have a large impact on the survivability of the cells. Goto *et al.* used micropatterned surfaces to control the directional growth of cells during culturing [12]. However, the interaction of cells as they fall towards the pattern or flow past the pattern were not investigated.

When dealing with droplet-substrate systems, two different regimes exist: the motion of droplets near a surface and the contact between droplet and surface. The forces acting on the system include gravity, inertia, and surface tension. The disproportionality of these forces can be used to simplify the continuity and conservation of momentum equations governing the fluid flow. For example, droplets traveling fast enough towards the surface will be dominated by inertia forces and therefore surface tension will play a smaller relative role. On the other hand, small droplets traveling slow towards the surface will be dominated by gravitational or surface tension forces and inertia can be neglected.

Two dimensionless parameters govern the dynamics of the system: the Bond number B_d and the viscosity ratio λ. The Bond number $B_d = \Delta\rho|\boldsymbol{g}|a^2/\gamma$ relates the gravitational force to the interfacial force where $\Delta\rho$ is the density difference between the two fluids, $|\boldsymbol{g}|$ is the magnitude of gravity, a is the droplet radius, and γ is the interfacial tension.

Sadhal *et al.* performed a comprehensive study on wall interactions with droplets and bubbles [27]. This study includes theory and experiments for many wall-droplet interactions including droplets *near* walls and droplets *attached* to walls.

Research has been done characterizing droplets or bubbles moving *parallel* to a flat surface, both experimentally [31] and computationally [19, 36]. Results from these studies

show that droplets or bubbles tend to move away from a wall when traveling parallel to it. Additionally, many studies have also been done on droplets and bubbles moving *perpendicular* towards a flat surface, again experimentally [16,17] and computationally [2,25,40]. However, the effect of substrate topology on the droplet are still not understood.

1.3. Computational studies on droplet-substrate interaction

The governing continuity and conservation of momentum equations are difficult to solve analytically in many cases and thus require numerical solutions. Until recently, most models have required at most two dimensions due to computing limitations. However, three-dimensional models now provide more realistic results for many difficult problems. Zhu *et al.* investigated the motion of droplets in bounded Stokes flow utilizing a boundary element method to investigate contractile flow through a nozzle [41]. Zinchenko *et al.* developed a boundary integral method to study the viscous interaction of multiple droplets [42].

While there are many simulations including viscous droplet motion in a viscous medium, the dynamics of droplets approaching or interacting with solid surfaces is a bit more unique. Ascoli *et al.* performed studies for droplets approaching flat substrates in the Stokes regime utilizing an axisymmetric boundary integral method [2]. They found that the commonly utilized thin-film lubrication equations may not be applicable when a dimple is formed under the droplet, which is often the case when approaching a flat surface. Yiantsios *et al.* also performed extensive work on quantifying the dimple's formation and magnitude [40]. They showed that for sufficiently long times, a dimple is always formed independent of the viscosity ratio, and the dimple radius is defined by its Bond number and droplet radius when the droplet approaches a rigid surface. The thin-film drainage and dimpling of finite Reynold's number droplets was also investigated by Quan who utilized a finite element method to simulate the approaching finite-inertia droplets [25].

For droplets approaching surfaces at low-*Re*, little work has been done. Legen-

dre *et al.* performed experimental and simple-modeling research on the bouncing of a buoyant droplet on a wall with finite Bond and Weber numbers [16, 17]. Simulations of droplets impacting and bouncing on surfaces have also been performed at small Weber numbers [20]; however, the quasi-static method deviated from experimental results when the Bond number was nonzero. Klaseboer *et al.* created a model for the impinging of droplets on a flat surface at high-*Re* [15].

Droplet impact on geometrically-patterned surfaces has been investigated experimentally for liquid droplets surrounded by air [14, 28, 35]. For square-shaped patterns, the textured pattern is shown to inhibit droplet spreading and deviates from the normal circular-shaped spreading pattern into diamond-shaped spreading pattern with the widest spreading occurring at directions parallel to the pattern [28]. A pattern of infinitely long ridges is shown to promote spreading in the direction parallel to the ridges and inhibit spreading in the transverse direction [14]. Computationally, research on droplets impacting patterned surfaces lacking. Reis *et al.* studied droplets impacting and impinging on porous surfaces [26]. Pasandideh *et al.* experimentally and computationally studied droplets impacting and solidifying on a steel plate [23]. All of these studies only looked at the spreading of droplets in contact with the substrate, and not the dynamics of droplets approaching the substrate. Indeed, in low-viscosity fluids such as air, the presence of a pattern on the substrate will produce negligible effects on the droplet prior to contact. In a viscous medium, the approach of the droplet cannot be ignored.

1.4. Summary of current research

The dynamics of viscous droplets surrounded by a viscous liquid impacting a patterned surface has not yet been analyzed computationally or experimentally. Using a three-dimensional Spectral Boundary Element method (SBEM), this research investigates the dynamics of a droplet moving near a patterned surface through a viscous medium in the Stokes (creeping flow) regime. Two studies are performed: the first looks at a droplet

approaching the patterned surface perpendicularly, and the second investigates a droplet moving parallel to the surface, across the pattern. The SBEM allows us to benefit from the spectral method's exponential convergence and numerical stability and the finite element method's ability to work with complicated geometries.

We consider a simplified substrate pattern of comparable size to the droplet in low-*Re*Stokes flow. The influences of Bond number, the relative size of droplet and substrate pattern, and substrate geometry on the droplet motion and deformation are investigated. The results from this study allow us to determine the effect of various substrate pattern characteristics on both the droplet dynamics as well as the surface stress which can be used to determine hydrophobic coating wear. The ability to control droplet dynamics with surface features has applications in droplet microfluidic devices and cell culturing.

This research has been presented at the ND/SD Engineering Research Summit in 2013, the ASME International Mechanical Engineering Congress and Exposition (IMECE) in 2013, and the ND Experimental Program to Stimulate Competitive Research (EPSCoR) conference in 2014. It will also be presented at the ASME Joint US-European Fluids Engineering Division Summer Meeting (FEDSM) in 2014 and will be submitted for publication in Microfluidics and Nanofluidics.

CHAPTER 2. MATHEMATICAL FORMULATION AND NUMERICAL METHODS

2.1. Problem description

Figure 1 illustrates a droplet surrounded by another fluid subject to gravity denoted as $\boldsymbol{g}$. The fluid inside the droplet, Fluid 1, has a viscosity of $\lambda\mu$ and a density of ρ_1 while the fluid outside the droplet, Fluid 2, has a viscosity of μ and a density of ρ_2. The surface tension between the two fluids is γ. Both fluids are considered Newtonian and incompressible. The droplet is falling due to gravity; that is, $\rho_1 > \rho_2$. The initial height of the droplet's centroid above the lowest part of the substrate is h.

The micropattern shown in Fig. 2 consists of two pillars of width w_1 and height w_2 separated by a distance w_3. The micropatterns extend into and out of the page a finite distance such that the total length of the pattern is equal to L. All of these lengths are scaled with the droplet size a. If not specified, $w_1 = 0.5$, $w_2 = 0.2$, $w_3 = 1$, and $L = 2$. The coordinate system is such that x denotes direction *across* the micropattern, y denotes direction parallel to the micropattern and z denotes direction perpendicular to the substrate. Theoretically, the substrate should extend to infinity in the x and y directions. This is approximated by choosing a substrate size large enough that it no longer affects the results near the center of the plate. The appropriate substrate size is determined later in section 4.1.4.

In this study, the surrounding fluid is quiescent; that is, no external flow field is imposed. The fluid flow and viscous stresses result from the motion of the interface between the droplet and surrounding fluid due to gravity. A dimensionless number is employed, the Bond number B_d, to quantify the relative importance of the surface tension and the body forces, in this case gravity,

$$B_d = \frac{(\rho_1 - \rho_2)|\boldsymbol{g}|a^2}{\gamma} \tag{2.1}$$

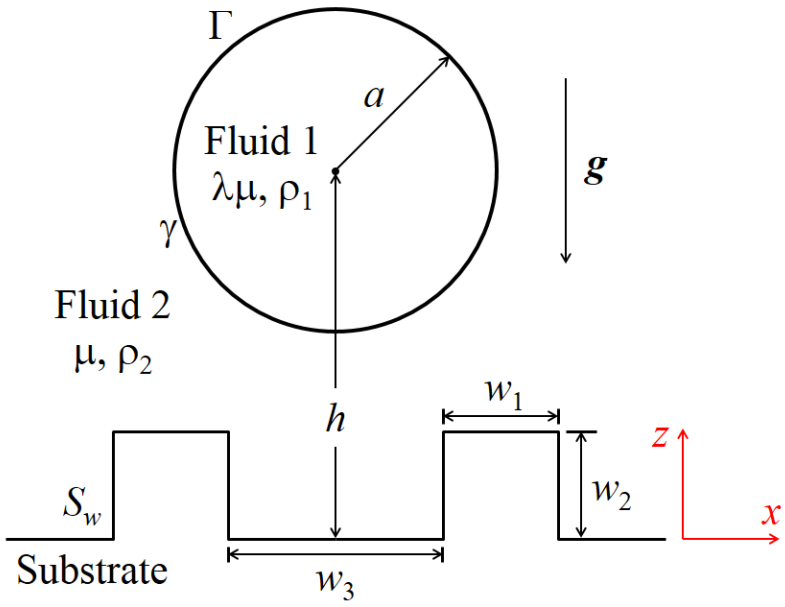

Figure 1. 2D schematic for a droplet subject to gravity above a micropatterned surface.

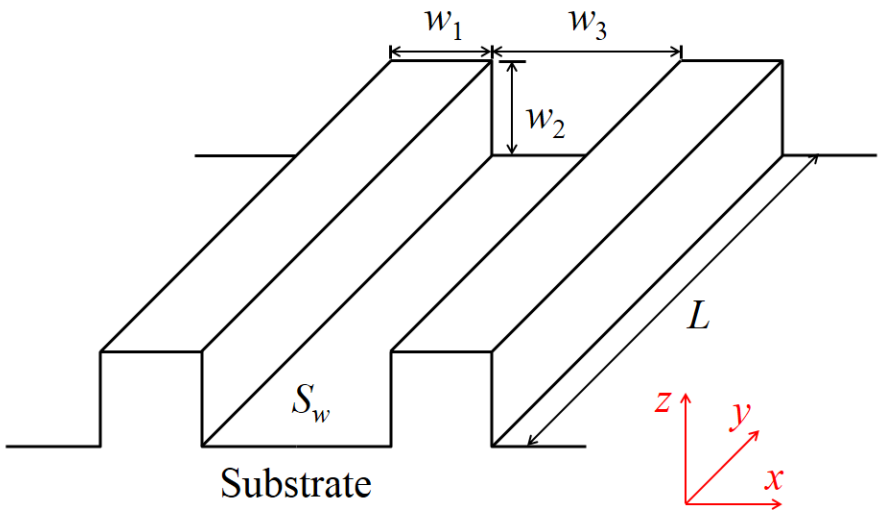

Figure 2. 3D schematic of the surface showing the finite depth L of the pillars and the Cartesian coordinate system. The $(0, 0, 0)$ coordinate is located directly between the two pillars at the bottom of the substrate.

Additionally, we have the Capillary number $Ca = \mu U/\gamma$, where U is a characteristic velocity (usually the terminal velocity of the droplet), that relates the viscous forces to surface tension, the Weber number $We = \rho_2 U^2 a/\gamma$ which relates the inertia forces to surface tension, and the Reynolds number $Re = \rho_2 U a/\mu$ which relates the inertia forces and viscous forces. We primarily work with the Bond number B_d in this study.

The length scale is the characteristic length a, the radius of the droplet, while the time scale is the buoyancy time scale $\tau_g = \mu/\Delta\rho g a$ where $\Delta\rho = |(\rho_2 - \rho_1)|$. Therefore, the velocity scale is $U = \Delta\rho g a^2/\mu$.

Theoretically, an extremely small time step can be used, and the simulations can run indefinitely. However, in practice, this is not reasonable due to compuational limitations and the simulation must be stopped at some point. In most cases, the simulation is stopped when the solutions (droplet profile, deformation D, or U_z) for adjacent time steps are negligibly different. However, due to the quick deceleration of the droplet when very close to the substrate, the time step may also cause the droplet interface to intersect with the substrate. In this case, the simulation is considered finished a few steps before the intersection.

2.2. Derivation of boundary integral equations

Due to negligible inertia (compared with viscous force and surface tension), *Re*and *We*are much smaller than unit and can be neglected. Therefore, the governing equations for fluid dynamics include the Stokes equations [36],

$$-\nabla p + \mu \nabla^2 \boldsymbol{u} = 0 \tag{2.2}$$

along with continuity,

$$\nabla \cdot \boldsymbol{u} = 0 \tag{2.3}$$

where p is the dynamic pressure, μ is the viscosity of the fluid, and $\boldsymbol{u}$ is the velocity vector.

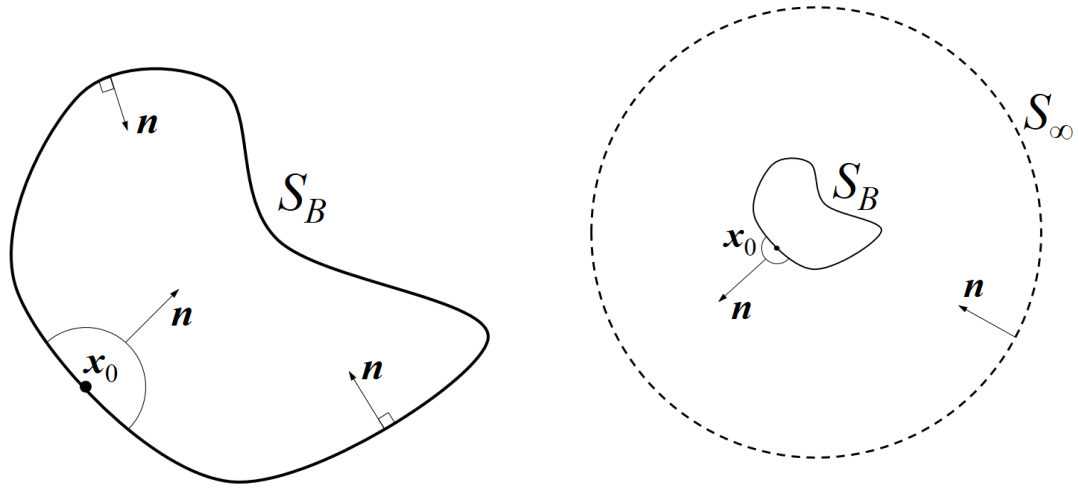

(a) (b)

Figure 3. Boundaries used in the boundary integral equations. (a) represents the "inner" equation 2.4 while (b) represents the "outer" equation 2.7.

Fundamental solutions S_{ij} and T_{ijk} for velocity and stress, respectively, are introduced into the Stokes and continuity equations 2.2 and 2.3. Then, the new equations are integrated over a volume of fluid bounded by a surface denoted S_B in Fig. 3(a). In this way, the velocity u_i at any point $\boldsymbol{x}_0$ on S_B can be defined as a Boundary Integral Equation (BIE),

$$u_i(\boldsymbol{x}_o) = -\frac{1}{4\pi\mu}\int_{S_B}\left(S_{ij}(\hat{\boldsymbol{x}})f_j(\boldsymbol{x}) - \mu T_{ijk}(\hat{\boldsymbol{x}})u_j(\boldsymbol{x})n_k(\boldsymbol{x})\right)\,\mathrm{d}S \tag{2.4}$$

This equation states that the velocity $\boldsymbol{u}$ at any point $\boldsymbol{x}_0$ on S_B is defined as the surface integral of the velocity and stress over all points $\boldsymbol{x}$ on the same boundary. Additional terms in the equation include the force vector $\boldsymbol{f}$, which is defined as $f_j(\boldsymbol{x}) = \boldsymbol{\sigma}_{jk}(\boldsymbol{x})n_k(\boldsymbol{x})$ and the normal vector $\boldsymbol{n}$ which always points *into* the volume enclosed by the surface. The fundamental solutions S_{ij} and T_{ijk} that we introduced in the beginning are defined given as [24],

$$S_{ij} = \frac{\delta_{ij}}{r} + \frac{\hat{x}_i\hat{x}_j}{r^3} \tag{2.5}$$

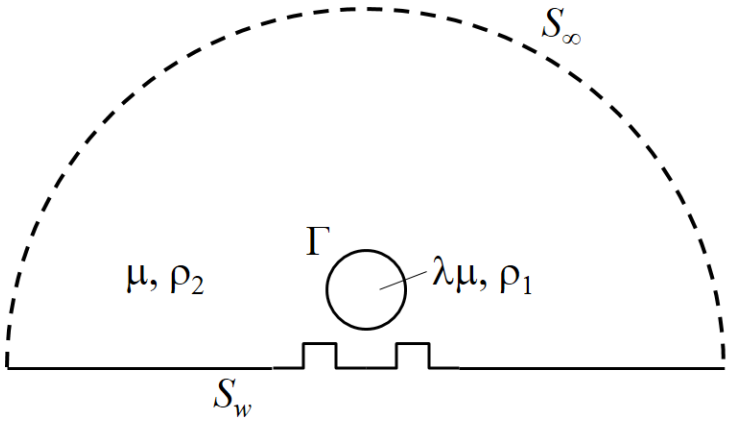

Figure 4. Schematic of the boundaries for a droplet suspended above a patterned surface.

$$T_{ijk} = -6\frac{\hat{x}_i\hat{x}_j\hat{x}_k}{r^5} \tag{2.6}$$

where $\hat{\boldsymbol{x}} = \boldsymbol{x} - \boldsymbol{x}_0$ and $r = |\hat{\boldsymbol{x}}|$ [24].

Equation 2.4 describes the fluid inside the boundary S_B and is thus called the "inner" equation. The equation which solves for the fluid outside of boundary S_B shown in Fig. 3(b) is determined by assuming a second boundary S_∞ infinitely far away from S_B with a known velocity $\boldsymbol{u}^\infty$. Doing this results in an "outer" equation similar to the inner equation

$$\boldsymbol{u}(\boldsymbol{x}_o) - 2\boldsymbol{u}^\infty(\boldsymbol{x}_o) = -\frac{1}{4\pi\mu}\int_{S_B}(\boldsymbol{S}\cdot\boldsymbol{f} - \mu\boldsymbol{T}\cdot\boldsymbol{u}\cdot\boldsymbol{n})\,\mathrm{d}S \tag{2.7}$$

where $\boldsymbol{n}$ points *into* the volume enclosed by surfaces S_B and S_∞. Note that the direction of $\boldsymbol{n}$ is opposite in equations 2.4 and 2.7. More detailed derivations of these boundary integral equations can be found in [13, 24].

For the problem specified in this study, a droplet is suspended near a substrate with semi-infinitely unbounded fluid surrounding it, shown in Fig. 4. The fluid interface is denoted as Γ and the solid wall is S_w. The BIEs shown here require a surface to be defined infinitely far away from the droplet. In practice, this is difficult to perform because using any finite distance will result in some amount of error. This surface also requires elements

for the Boundary Element Method (BEM) shown later which will increase computational cost. However, this can be resolved by introducing "disturbed" velocity and force, $\boldsymbol{u}^D = \boldsymbol{u} - \boldsymbol{u}^\infty$ and $\boldsymbol{f}^D = \boldsymbol{f} - \boldsymbol{f}^\infty$. Based on the fact that S_∞ is far away from the droplet, $\boldsymbol{u}^D$ and $\boldsymbol{f}^D$ are zero on S_∞ and the integration over this surface is zero. The inner equation 2.4 is altered to [24],

$$\boldsymbol{u}^D(\boldsymbol{x}_o) = -\frac{1}{4\pi\mu}\int_{\Gamma+S_w}\left(\boldsymbol{S}\cdot\boldsymbol{f}^D - \mu\boldsymbol{T}\cdot\boldsymbol{u}^D\cdot\boldsymbol{n}\right)\,\mathrm{d}S \tag{2.8}$$

Now, equation 2.4 is applied to the flow inside the droplet, its sign changed due to the direction of $\boldsymbol{n}$, and it is subtracted from equation 2.8. This results in a new BIE describing the system [24],

$$\begin{aligned}
&\Omega\boldsymbol{u}(\boldsymbol{x}_0) - \Omega_0\boldsymbol{u}^\infty(\boldsymbol{x}_0) = \\
&-\int_\Gamma \left[\boldsymbol{S}\cdot(\Delta\boldsymbol{f} - \boldsymbol{f}^\infty) - \mu\boldsymbol{T}\cdot(\boldsymbol{u}(1-\lambda) - \boldsymbol{u}^\infty)\cdot\boldsymbol{n}\right] dS \\
&+\int_{S_w}\left[\boldsymbol{S}\cdot\boldsymbol{f}_2 - \lambda\mu\boldsymbol{T}\cdot\boldsymbol{u}_2\cdot\boldsymbol{n}\right] dS
\end{aligned} \tag{2.9}$$

where $\Omega = 4\pi\mu(1+\lambda)$ and $4\pi\mu$ for $\boldsymbol{x}_0$ on Γ and S_w, respectively and $\Omega_0 = 4\pi\mu$ on all interfaces. It is important to note that, while S_∞ is no longer relevant, the surface S_w is still infinite and must be large enough to minimize error.

The boundary conditions at the droplet-surrounding fluid interface are,

$$\boldsymbol{u} = \boldsymbol{u}_1 = \boldsymbol{u}_2 \qquad \text{on boundary } \Gamma \tag{2.10}$$

$$\Delta\boldsymbol{f} \equiv \boldsymbol{f}_2 - \boldsymbol{f}_1 = \gamma(\nabla\cdot\boldsymbol{n})\boldsymbol{n} + (\rho_2 - \rho_1)(\boldsymbol{g}\cdot\boldsymbol{x})\boldsymbol{n} \qquad \text{on boundary } \Gamma \tag{2.11}$$

where the subscripts "1" and "2" refer to the fluids defined in Fig. 1. The first term on the right hand side of equation 2.11 contains force due to interfacial tension, while the second term corresponds to body forces. The vector $\boldsymbol{n}$ is the unit normal pointing *out* of

the interfaces – towards the suspending fluid for both the droplet and the substrate. On the substrate surface S_w, a no-slip boundary condition is applied,

$$\boldsymbol{u}_2 = 0 \qquad \text{on boundary } S_w \tag{2.12}$$

Equation 2.9 is a system of Fredholm equations of mixed kinds due to the different boundary conditions on each boundary.

2.3. Spectral boundary element method

Muldowney and Higdon describe in detail how the Spectral Boundary Element method (SBEM) is used to solve the BIEs from section 2.2 [21]. The SBEM provides exponential convergence and numerical stability combined with the finite element method's ability to work with complicated geometries. Additionally, the SBEM does not succumb to disadvantages of the spectral methods such as dense systems (because the BIEs are always dense regardless of the discretization). Dimitrakopoulos and Higdon used the SBEM to study droplet displacement from surfaces [4, 5, 6, 7, 8]. Wang and Dimitrakopoulos have also used SBEM to study droplet motion parallel to a surface and Dimitrakopoulos also studied droplets suspended in a flow [10, 36].

For the SBEM, the entire boundary is divided into a moderate number of quadrilateral spectral elements N_E. Each of these spectral elements is then divided into spectral points (e.g. $N_B \approx 10$) in each direction. The droplet boundary is divided into approximately 6 or 10 elements. The pattern on the substrate is also discretized into elements, approximately one element for each flat surface. The infinite substrate is discretized into multiple elements, approximately eight, to reduce error due to large mesh size. Figure 5 shows this discretization for (a) an undeformed droplet and (b) a deformed droplet.

Lagrangian interpolation is used to find the geometrical and physical properties over the entire droplet interface. To do this, each element is mapped onto a local parametric variable system of ξ and η. These variables are the zeros of some orthogonal polynomials,

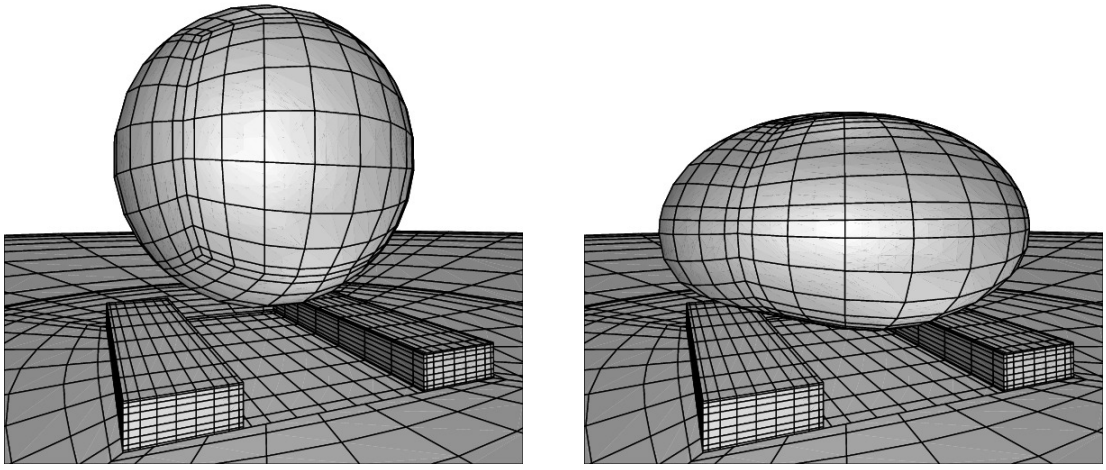

(a) (b)

Figure 5. Geometry and discretization of a droplet above the substrate: (a) the initial spherical shape of the droplet, and (b) the deformed droplet shape at time $t = 5$ for a droplet with $B_d = 10$, $\lambda = 0.2$, $h = 1.3$.

such as Legendre or Chebyshev polynomials, on the domain of [-1, 1]. For N_B basis points, the geometry $\boldsymbol{x}$ is,

$$\boldsymbol{x}(\xi,\eta) = \sum_{i=1}^{N_B}\sum_{j=1}^{N_B} \boldsymbol{x}(\xi_i,\eta_j) h_i(\xi) h_j(\eta) \tag{2.13}$$

where $h_i(\xi)$ and $h_j(\eta)$ are the $(N_B - 1)$-order Lagrange interpolant polynomial. A similar relation is also used for $\boldsymbol{u}$ and $\boldsymbol{f}$.

With the geometry and physical properties properly discretized, they can be substituted into the BIEs with a requirement that the integral equations must be satisfied at the basis points $\boldsymbol{x}_0(\xi_i,\eta_j)$ where $i,j = 1,\ldots,N_B$ on each spectral element. This results in a linear system of $3N_E N_B^2$ equations to solve,

$$\boldsymbol{u} = \boldsymbol{A}\boldsymbol{f} + \boldsymbol{B}\boldsymbol{u} \tag{2.14}$$

where $\boldsymbol{A}$ and $\boldsymbol{B}$ are defined as the integrals of kernels $\boldsymbol{S}$ and $\boldsymbol{T}$ and the basis functions over the set of surface elements. These numerical integrations for $\boldsymbol{A}$ and $\boldsymbol{B}$ are best performed

by Gauss-Legendre quadrature. Combining the BIEs with the boundary data at $N_E N_B^2$ basis points yields a set of $3N_E N_B^2$ equations and $3N_E N_B^2$ unknowns which can be solved using Gaussian elimination.

CHAPTER 3. INTERFACIAL DYNAMICS FOR SUSPENDED DROPLETS NEAR SURFACES

3.1. Dimensionless analysis

The interfacial dynamics for Stokes flow for a droplet falling towards a surface is governed by dimensionless numbers for the viscosity ratio, $\lambda = \mu_1/\mu_2$, and the Bond number, B_d given in Eqn. 2.1. The Bond number describes the opposing forces of gravity, $\Delta\rho|\boldsymbol{g}|a^2$, and interfacial tension, γ, where a is the characteristic length (i.e. the radius) of the droplet. Gravitational force pulling the droplet towards the substrate is contested by the surface tension attempting to keep the droplet spherical. At some point, these forces will equalize and the droplet will no longer deform.

Figure 6(a) shows the 2D evolution of deformation of a droplet approaching a patterned substrate. In order to compare droplets with different properties, it is helpful quantify the amount of deformation D,

$$D = \frac{l_1 - l_2}{l_1 + l_2} \tag{3.1}$$

where l_1 and l_2 are the longest and shortest distances from the centroid of the deformed droplet to the droplet interface respectively, shown in Fig. 6(b). For this problem, the characteristic length a is used as the dimensionless length scale, the velocity scale is $U = \Delta\rho|\boldsymbol{g}|a^2/\mu$, the force scale is $P = \mu U/a = \Delta\rho|\boldsymbol{g}|a$, and the time scale is $T = U/a = \Delta\rho|\boldsymbol{g}|a/\mu$.

3.2. Time-integration algorithm and smoothing method

The chosen problems examine a droplet suspended above a patterned surface in two situations: the droplet slowly falling perpendicular to the surface and the droplet slowly falling parallel to the surface. The governing Stokes equation and continuity have been reduced to the BIE in equation 2.9 and the boundary conditions given in equations 2.10, 2.11, and 2.12. The Spectral Boundary Element method in section 2.3 is used to solve this system by first discretizing the domain into a set of spectral elements N_E with N_B^2 Lobatto

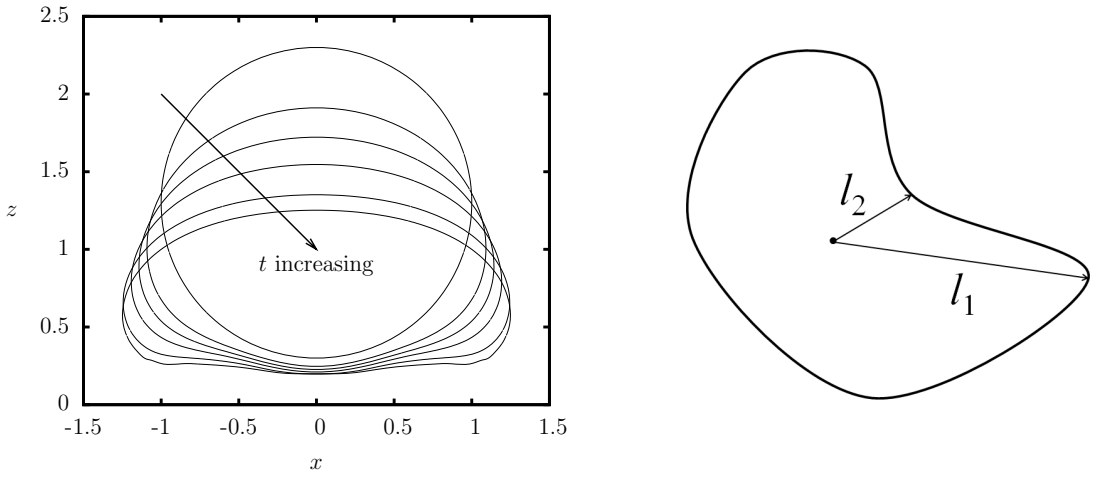

(a) (b)

Figure 6. (a) Time evolution of deformation profiles for a droplet approaching a patterned substrate. (b) An arbitrarily deformed droplet with the two lengths l_1 and l_2 used to quantify the amount of deformation.

basis points on each element. The SBEM is then used to solve for the velocity and forces on each boundary. However, since the substrate is not moving, the velocity is known to be zero and only the force needs to be determined. On the droplet interface, the interfacial force $\Delta \boldsymbol{f}$ is a known boundary condition based on the amount of deformation the interface is undergoing, and thus only the velocity needs to be determined. This method so far only solves for the velocity or force at a given time step, and the procedure for moving forward in time will be discussed here.

The transient droplet shape is found by using a fourth-order Runge-Kutta method to solve the kinematic relation,

$$\frac{d\boldsymbol{x}}{dt} = (\boldsymbol{u} \cdot \boldsymbol{n})\boldsymbol{n} \tag{3.2}$$

where $\boldsymbol{x}$ is the discretized droplet points and $\boldsymbol{n}$ is the normal vector at each point. First, the interfacial velocity $\boldsymbol{u}$ of the known shape $\boldsymbol{x}(t)$ from the BIE in equation 2.9 is determined. Next, the discretized points on the droplet interface are moved forward in time by Δt

according to each point's current position and velocity,

$$\boldsymbol{x}(t + \Delta t) = \boldsymbol{x}(t) + \Delta t(\boldsymbol{u} \cdot \boldsymbol{n})\boldsymbol{n} \tag{3.3}$$

It is important to note that so far there is no constraint holding the spectral elements together. Therefore, after some time, the discontinuities existing at the edge of each spectral element will break up the moving domains.

To resolve this issue, a first-order smoothing method refines the computed droplet shape and maintains continuity of the position of the element and the normal and tangent vectors at the edges of the elements [37]. Briefly, this is done by first averaging the position of the points along each spectral element edge. The geometry is updated and the geometric properties are recalculated. Next, the unit tangent vectors is calculated at each point along the element edges and are similarly averaged for adjacent elements. This also causes the unit normal vectors to be identical along the edges. Lastly, the first-order derivatives are determined and updated using the relation $|\partial \boldsymbol{x}/\partial \xi|^{new} = |\partial \boldsymbol{x}/\partial \xi|^{old}$ and similarly for η.

Once these edges have been updated, the entire drop shape must be smoothed. This is done by first generating interior Jacobi points from the N_B^2 Lobatto basis points on each element. These Jacobi points are then combined with the smoothed position, tangent, and first-order derivatives previously found to create a new set of N_B^2 Lobatto points which are smoothed. The new Lobatto points are created using a two-dimensional Hermitian interpolation involving two nested one-dimensional Hermitian interpolations derived by Dimitrakopoulos [9]. In addition to smoothing the position, tangent vector, and first-order derivative along the edges, this method also informally smooths the second-order derivative, the curvature of the droplet. The smoothing method in its entirety is described by Wang [37].

CHAPTER 4. DROPLET FALLING NORMAL TO A PATTERNED SUBSTRATE

4.1. Parameter determination

The numerical method is verified for several parameters including time step, initial height, geometry discretization, and substrate radius for a droplet approaching a flat substrate. Two measures of performance used are the droplet's deformation, D defined in equation 3.1, and centroid velocity perpendicular to the substrate, U_z.

4.1.1. Time step size

The time step was justified by simulating a droplet approaching a substrate for three different time steps and comparing the deformation between them at a single point in time. Figure 7 shows the results from this test. We observe that all three time steps resulted in nearly identical deformation. Due to this, a time step of $\Delta t = 10^{-3}$ was deemed sufficient for the calculations. However, the time step can be varied during the simulation to speed up calculations while the droplet is far away from the substrate and improve resolution when the droplet approaches the substrate.

4.1.2. Initial height

The initial height of the droplet centroid was verified by simulating a droplet approaching a substrate for four different heights of $h_0 = 3, 5, 10, 15$. The relative error in deformation between the different heights was calculated when the droplets reached a height of $h = 1$. The results from this verification test for deformation are shown in Fig. 8. As h_0 increases, the assumption of a spherical droplet becomes more valid and thus, the deformation as the droplet approaches the substrate is more precise. Figure 9 shows that the profiles for three initial height simulations are identical near the substrate. From these results, an initial height of $h_0 = 10$ was chosen to be sufficient for simulations. Using similar approaches, Ascoli *et al.* showed that an initial height of 15 radii above the substrate is sufficiently large to assume the droplet is spherical in their study [2].

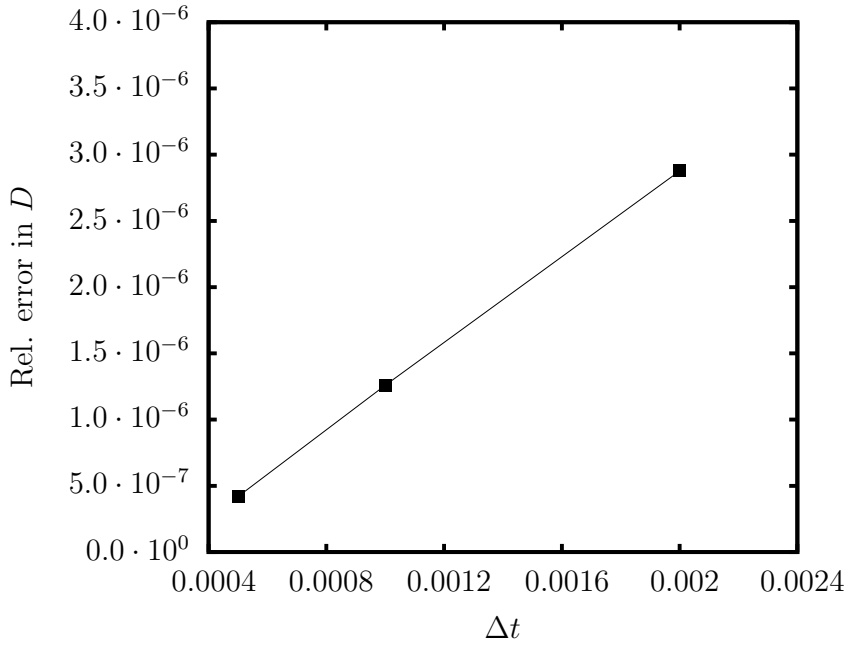

Figure 7. Relative error in deformation versus time step Δt. $\Delta t = 2d - 4$ serves as the base for the relative error of the other Δt. The parameters chosen for this verification were $B_d = 2$, $\lambda = 0.2$, $h_0 = 1.3$.

4.1.3. Discretization size

The geometry is discretized into a few spectral boundary elements N_E. Each of these elements has a basis number N_B of collocation points in which the variables $\boldsymbol{u}$ and $\boldsymbol{f}$ are defined. Thus, the total number of spectral points in the geometry is $N = N_E {N_B}^2$. An example of this discretization is shown in Fig. 5. The geometry discretization was verified by changing the number of basis points $N_B = 7, 8, 10, 12, 14, 15$ and calculating the relative error between simulated results. The results from the geometry discretization verification method are shown in Fig. 10. A moderate basis number of $N_B = 10$ corresponding to $N = 2900$ was chosen to be sufficient for most situations. Unlike the time step, the basis number cannot be changed mid-simulation and thus more consideration is taken to ensure sufficient accuracy.

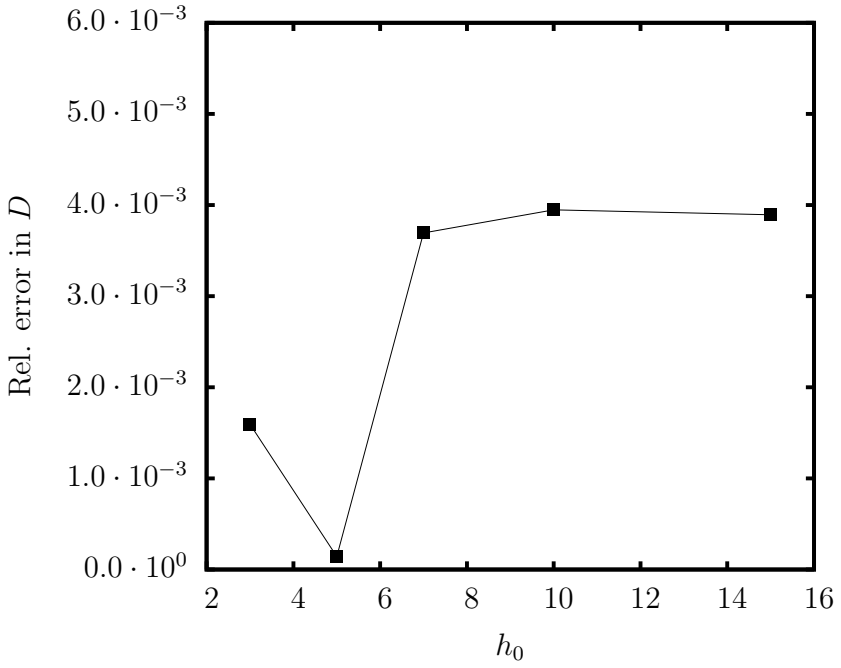

Figure 8. Relative error in deformation versus initial height h_0. $h_0 = 15$ serves as the base for the relative error of the other h_0. The parameters chosen for this verification were $B_d = 2.5$, $\lambda = 0.5$.

4.1.4. Substrate radius

Due to the nature of finite element, the substrate cannot be truly infinite. Thus, it is important to choose a substrate which is large enough to approach infinity but still reasonable for computations. To chose a sufficient substrate radius, simulations were run with substrate radii of 20, 30, 40, and 50 and the relative error in deformation between simulated results was calculated when the droplets reached a height of $h = 11$. The substrate radius of 50 serves as the base for the relative error calculation. The results from this verification are shown in Fig. 11. It is clear that a larger substrate radius will produce more precise results. However, larger substrates require more elements to ensure accuracy and thus require more computational effort; a typical trade-off situation. Due to the relatively low amount of error for all substrate radii considered, a substrate radius of 20 was chosen for further simulations.

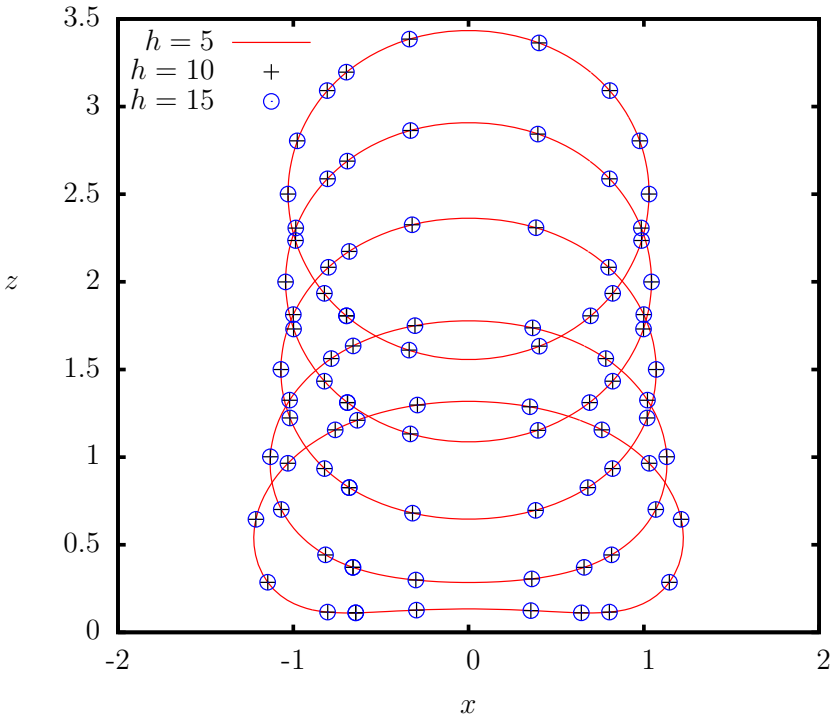

Figure 9. Droplet profiles at $h = 2.5, 2.0, 1.5, 1.0, 0.633$ for initial heights $h_0 = 5, 10, 15$. The parameters chosen for this verification were $B_d = 2.5$, $\lambda = 0.5$.

4.2. Validation of numerical method

The numerical method was validated against experimental studies and simulations from literature. Parameters from simulations of droplets falling towards a flat substrate by Ascoli *et al.* [2] were used to validate our spectral boundary element method. The velocity towards the plate for both our simulation as well as Ascoli *et al.* is shown in Fig. 12. The droplet profiles were also compared with Ascoli *et al.* in Fig. 12 and found to be nearly identical.

Experiments were performed for droplets approaching a flat plate and compared with the SBEM simulation results. The experiment was performed using a First Ten Angstroms FTA1000B drop shape analyzer. A millimeter size water droplet was released in silicone oil with slightly lower density. The droplet approached a hydrophobic-coated surface and images were captured at approximately 60 fps. Surface tension and viscosity ratios were calculated using manufacturer data. An experimental Bond number B_d and viscosity

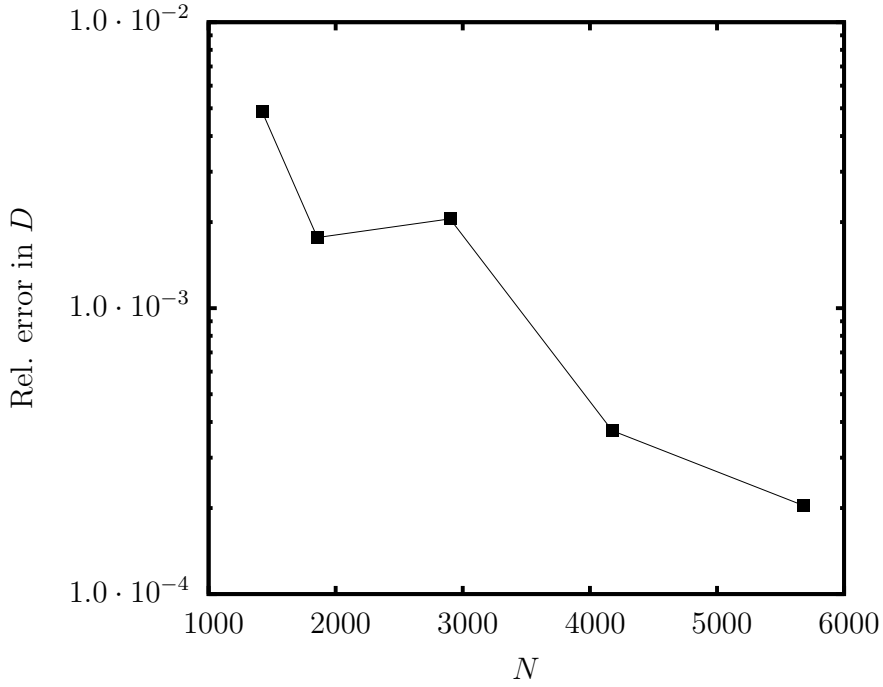

Figure 10. Relative error in deformation versus number of spectral points $N = N_E {N_B}^2$ for several different numbers of basis points $N_B = 7, 8, 10, 12, 14, 15$. $N_B = 15$ serves as the base for the relative error of the other N_B. The parameters chosen for this verification were $N_E = 29$ ($N_{droplet} = 10$, $N_{substrate} = 19$), $B_d = 2$, $\lambda = 0.2$, $h_0 = 1.3$.

ratio λ were calculated with these parameters and used for the simulation. Simulation results were then dimensionalized using the experimental parameters. The droplet profile at its maximum amount of deformation along with some important parameters is shown in Fig. 14. The largest shape very closely matches the simulation results, but is not exact. Deformation of the experimental droplet was quantified by importing droplet boundary data, calculating a centroid using the average of x and y data, and evaluating D from equation 3.1. The D-h relationship for both experiment and simulation is shown in Fig. 15. Consistent with the droplet profile, the deformation for both the experiment and simulation are nearly identical when the droplet is close to the substrate. However, the simulation over-predicts the deformation when the droplet is further away from the substrate. We believe this is due to the large size of the droplet resulting in non-negligible amounts of inertia.

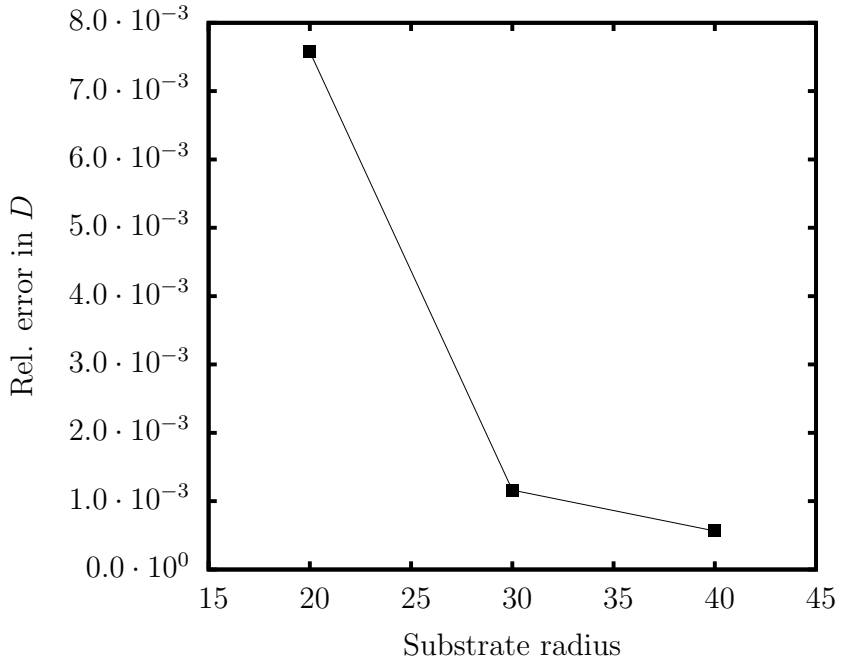

Figure 11. Relative error in deformation versus substrate radius. A substrate radius of 50 serves as the base for the relative error of the other substrate radii. The parameters chosen for this verification were $B_d = 1$, $\lambda = 0.3$, $h_0 = 15$

Since the simulation assumes creeping flow with zero inertia, this may be responsible for the discrepancy.

4.3. Results & discussion

The behavior of the droplet free falling towards the substrate is computed using the methods described. The droplet is at terminal velocity and moves towards the substrate since $B_d > 0$ ($\rho_1 > \rho_2$). The case where the droplet moves away from the substrate (i.e. , $B_d < 0$) is not computed in this study. The effect of different parameters such as B_d, droplet radius, and substrate parameters w_1, w_2 and w_3 is shown in the proceeding sections.

4.3.1. Influence of Bond number

Two-dimensional profiles of different B_d droplets on the x-z plane are shown in Fig. 16. The deformation of the droplet is computed as a function of height h for different B_d and is shown in Fig. 17. Additionally, the velocity of the droplet as a function of h

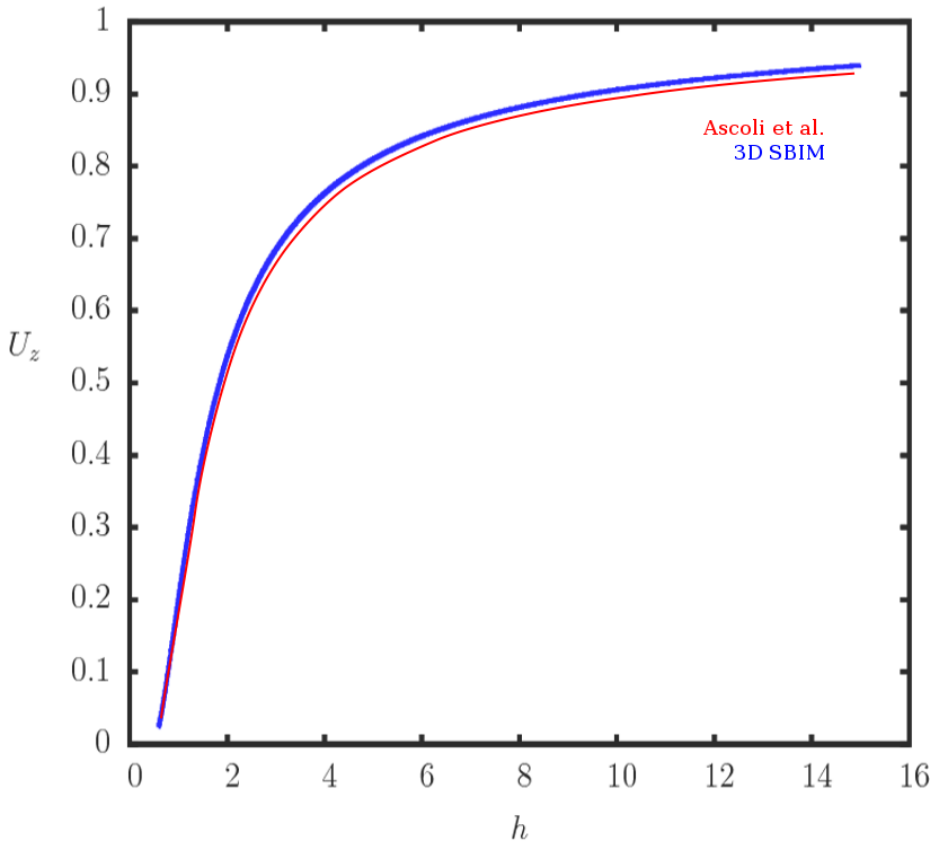

Figure 12. Droplet velocity U_z as a function of height h for $B_d = 3.75$, $\lambda = 1$, and $h_0 = 15$ [2].

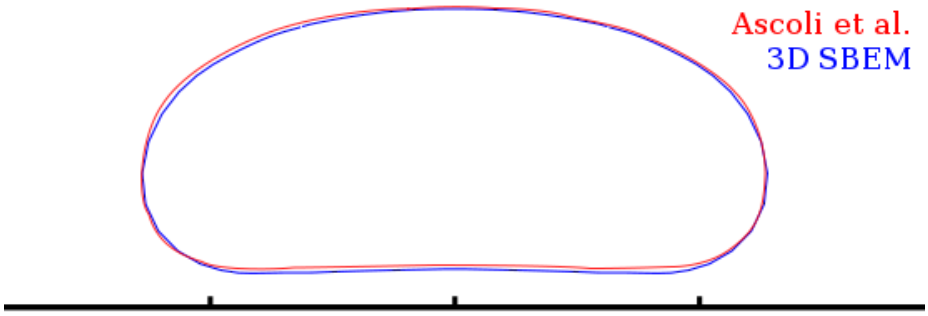

Figure 13. Final droplet profile for $B_d = 3.75$, $\lambda = 1$, and $h_0 = 15$ [2].

is shown in Fig. 18. The droplet height h is measured between the droplet centroid and the substrate surface at $z = 0$. Since a remained constant, B_d was varied by changing the surface tension γ. It is clear that the overall deformation of the droplet increases as B_d is increased. This is described by equation 2.1; as B_d increases, the gravity force dominates over the surface tension force and the droplet deforms more. The droplet velocity is

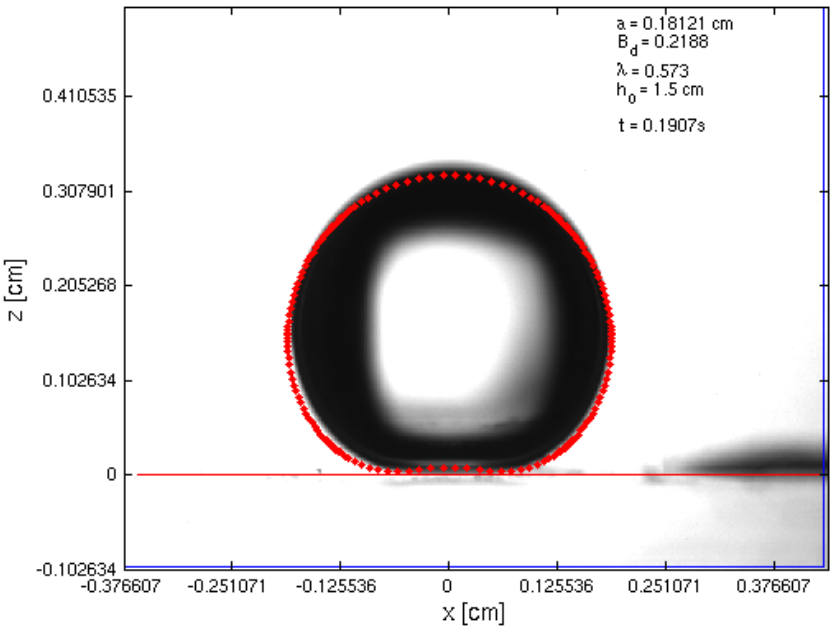

Figure 14. Droplet shape at the point of maximum deformation. The red dotted curve is the SBEM simulated profile.

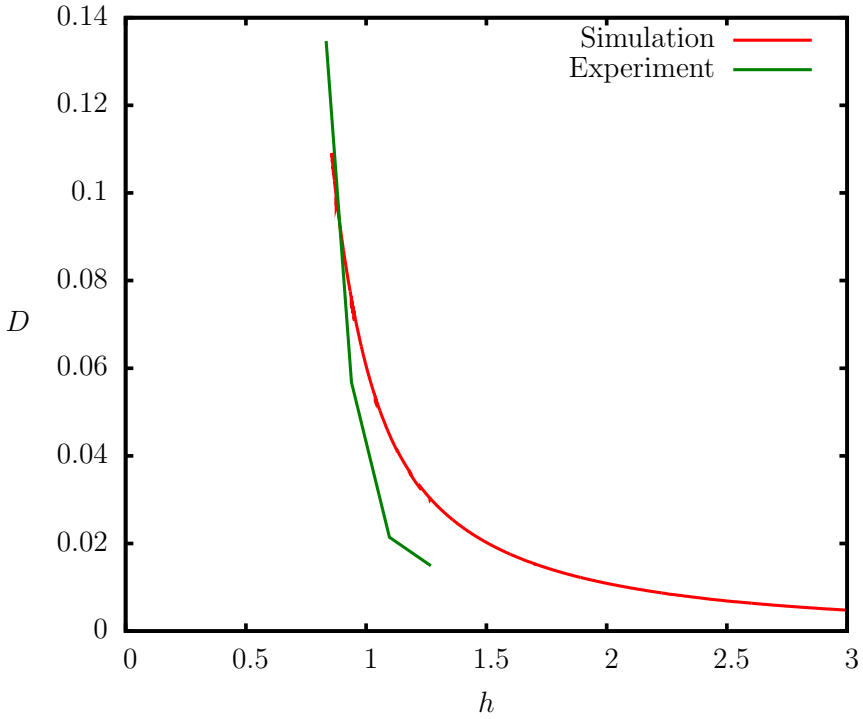

Figure 15. Droplet deformation D as a function of height h for both the simulated and experimental data.

relatively unaffected by variations in B_d.

Ascoli *et al.* use the distance h_{min}, that is the smallest vertical distance between the droplet and the substrate, as a potentially interesting parameter to describe droplet dynamics [2]. A plot of h_{min} versus h for various B_d is shown in Fig. 19(a). Viewing the y-axis, as B_d increases, h_{min} is larger at any given h. Additionally, viewing the x-axis, as B_d increases, the final centroid location of the droplet is closer to the substrate. This is a interesting contradiction: while the final centroid location is closer to the substrate, the h_{min} is actually larger. Thus, larger B_d droplets tend to squeeze flatter while remaining levitated further above the substrate.

The stresses on the substrate were also investigated to determine the effect of varying B_d. Figure 20 shows the normal and shear stress distributions for a three different B_d at the time of maximum stress. Note that the z-axis has been exaggerated to show detailed stresses on the pattern. The peak stress at this time is located near the corners of the pattern. Despite having radically different deformation magnitudes, the stress magnitude and distribution on the substrate is nearly identical.

It is also interesting to look at the peak stress as a function of h to find if varying B_d has any discernible effect on *when* the maximum stress occurs. Figures 21 and 22 show the maximum normal and shear stress as functions of h. Increasing B_d caused both the maximum normal and shear stresses to occur at a smaller h. The peaks retained the same magnitude and the overall maximum stress-h shape was similar for all tested B_d. This is an important observation for possible use with coatings: the droplet properties don't seem to affect the magnitude of stress on the substrate. Droplets with high amounts of deformation will theoretically produce similar amounts of stress as a solid sphere.

The deformation of the droplet as a function of droplet height h for different B_d is shown for both patterned and smooth substrates in Fig. 23. Each droplet started from a height of 1.3 from the substrate and as it approached the substrate it deformed. We

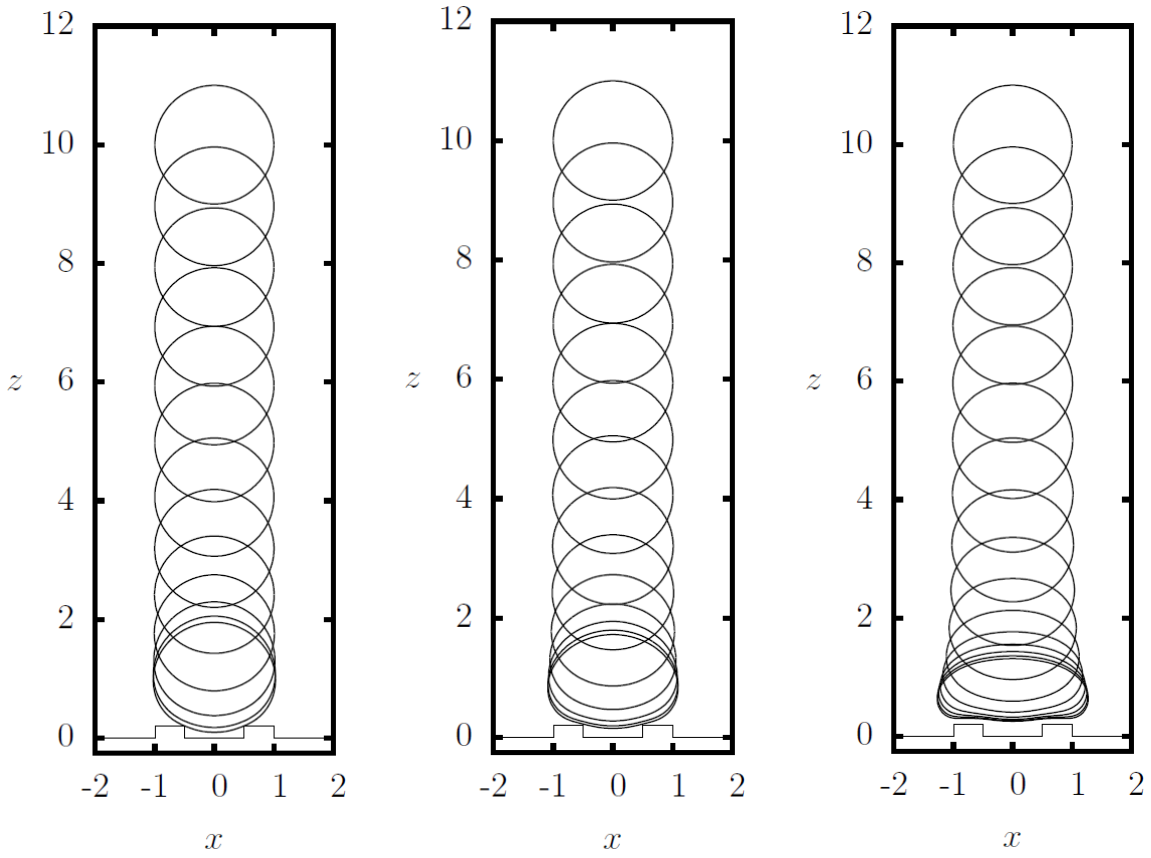

Figure 16. 2D droplet profiles for (a) $B_d = 0.25$, (b) $B_d = 1$, and (c) $B_d = 4$ for $\lambda = 0.5$ and $h_0 = 10$.

found that the droplet deforms more at the existence of micro-patterns if we measure the deformation at the same height. It seems that after being dropped from the initial height, the patterned curves tend to split off away from the $B_d = 2$ which acts as a sort of anti-asymptote on this plot. This phenomenon does not appear clearly in the smooth curves. Additionally, as B_d increases, the difference in the D-h relationship between the droplet falling on a patterned substrate or a smooth substrate becomes greatly magnified.

4.3.2. Influence of droplet radius

Equation 2.1 shows that the radius of the droplet also directly affects the B_d. However, since the undeformed droplet radius a is used as the dimensionless length scale, and

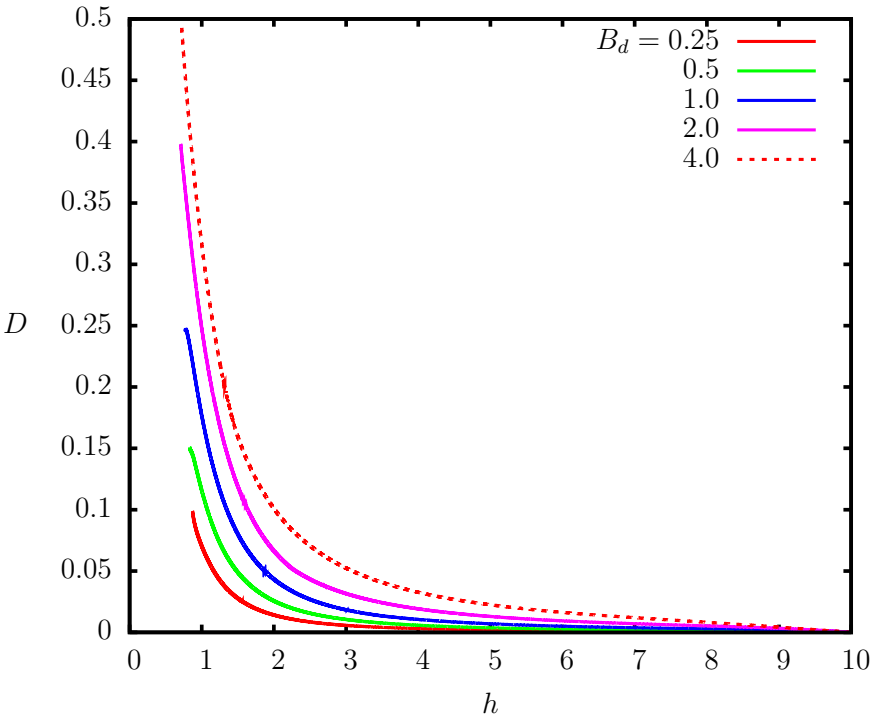

Figure 17. Droplet deformation D as a function of height h and Bond number B_d for $\lambda = 0.5$ and $h_0 = 10$.

thus the relative size of the droplet and substrate must be altered by changing the substrate size instead. In addition to scaling the substrate size, B_d and the dimensionless scales must also be changed to account for the "changing droplet radius". For example, to study a droplet *half* of the original radius, the substrate is scaled up by a factor of 2 and B_d is scaled down by a factor of 0.25. Figure 24 shows the two-dimensional profiles of different sized droplets approaching the patterned surface.

Figure 25 shows how varying the droplet radius changes the D-h relationship while Fig. 26 shows the U_z-h relationship. Since the dimensionless scales have been changed, it is important to introduce units to compare the results from different simulations. Properties from a typical water-oil experiment were used to scale the axes of Figs. 25 and 26. The fluid properties were taken from the experiments performed in section 4.2. The chosen length scales are $a = 0.05$, 0.10, and 0.20 cm for cases 1, 2, and 3, respectively. This results in velocity scales of $u = 17.84$, 71.36, and 285.42 cm/s, respectively. As the relative droplet

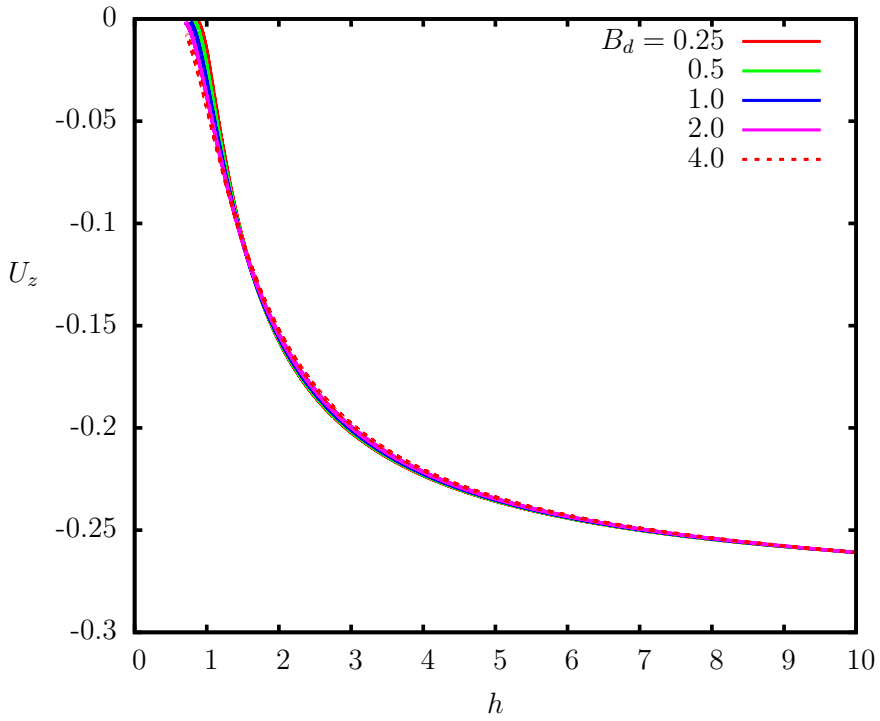

Figure 18. Droplet velocity U_z as a function of height h and Bond number B_d for $\lambda = 0.5$ and $h_0 = 10$.

size becomes larger and subsequently B_d becomes larger, the deformation of the droplet increases. If we keep making the droplet larger and larger, the pattern on the substrate will be extremely small relative to the droplet, and the droplet will behave as if it is a flat-plate. Additionally, as the relative droplet size decreases and B_d decreases, the surface tension forces dominate and thus the droplet deforms less.

A plot of h_{min} versus h for various droplet sizes is shown in Fig. 27. Interestingly, these results show an opposite trend to varying B_d. For any given centroid height h, the larger and more deformable droplet actually reaches closer to the substrate than the smaller droplet. Additionally, even though the largest droplet starts much farther away from the substrate than the smallest droplet, each droplet approaches similar final values for h_{min} and centroid height h.

The stresses on the substrate were also investigated to determine the effect of varying relative droplet size. The resulting stress distributions are shown in Fig. 28. For a small

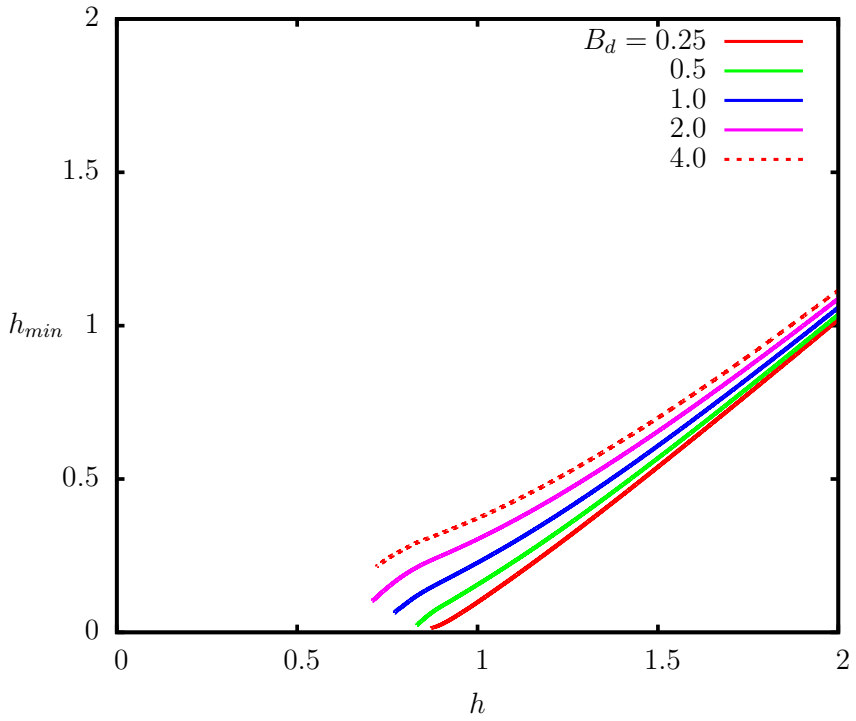

Figure 19. Minimum height h_{min} as a function of height h and Bond number B_d for $\lambda = 0.5$ and $h_0 = 10$.

droplet shown in Fig. 28(a) and (b), the stress magnitude is much smaller and is focused on a small part of the substrate beneath the droplet. For a large droplet in Fig. 28(e) and (e), the stress magnitude is larger and is distributed over the entire substrate rather than concentrated on the inside of the pattern. Additionally, there is less shear stress between the pillars more shear stress outside of the pillars for larger droplets compared to smaller droplets.

Figures 29 and 30 show the maximum normal and shear stress as functions of h for the different droplet sizes. Again, the axes were scaled with units in order to properly display the different droplet sizes on the same figure. Clearly varying the droplet size drastically changes the peak stress magnitude and peak value of h. Larger droplets result in larger stress magnitudes while smaller droplets result in small stress magnitudes.

4.3.3. Influence of pattern parameters

The different substrate parameters w_1, w_2 and w_3 are varied to see the effect of

different patterns on the droplet dynamics. For a specified liquid-liquid system, these are the parameters we hope to control.

The pattern height, w_2, is the first substrate parameter to be adjusted. The case in which $B_d = 1$, $w_1 = 0.5$, $w_2 = 0.2$, $w_3 = 1$ serves as the control simulation. Two more cases in which the pattern is taller ($w_2 = 0.6$) and shorter ($w_2 = 0.06$) are simulated. Final droplet shapes are shown in Fig. 31 for the tested B_d and compared with a flat plate solution. It is clear that the existence of even a very short pillar effectively eliminates the dimple seen in a flat-plate solution. As the pillar gets taller, the droplet protrudes further between the pillars. The variations in D and U_z versus h are shown in Figs. 32 and 33 and h_{min} versus h shown in Fig. 34. From these figures, it is clear that the droplet deforms less when the pillars are taller. The velocity is also smaller for a taller pattern. As the pillars get shorter, the solution expectedly approaches that of a flat substrate. The minimum height h_{min} follows the same trajectory for each pattern height, but ends at a different height due to the higher pattern.

The pattern width, w_3, is varied next. The case in which $B_d = 1$, $w_1 = 0.5$, $w_2 = 0.2$, $w_3 = 1$, serves as the control simulation. Two more cases in which the pattern is wider ($w_3 = 1.5$) and narrower ($w_3 = 0.5$) are simulated. Profiles of the droplet are shown in Fig. 35. As the pillars get further apart, the solution approaches that of a flat-plate. The variations in D and U_z versus h are shown in Fig. 36 and 37 and h_{min} versus h shown in Fig. 38. As the gap in the pattern gets narrower, the droplet must squeeze between the pillars which results in a slightly higher value of D at any given h. Additionally, a narrower gap impedes the motion of the droplet resulting in a lower velocity. As w_3 gets large enough, the solution approaches that of a flat substrate and the pillars have no noticeable effect. The minimum height h_{min} follows nearly the same trajectory for each value of w_3 with only slightly higher h_{min} for narrow gaps.

The pattern length, L, is another parameter of importance. The case in which $B_d = 1$,

$w_1 = 0.5$, $w_2 = 0.2$, $w_3 = 1$, $L = 1$ serves as the control simulation. Four more cases in which the pattern is longer ($L = 1.5, 2, 2.5$) and shorter ($L = 0.5$) are computed to see the variations in D and U_z versus h in Figs. 39 and 40 and h_{min} versus h in Fig. 41. The pattern length appears to have very little impact on the numerical properties shown here. Even the droplet profiles are nearly identical when viewed in both the x-z and y-z directions. The case when $L = 0.5$ showed the largest discrepancy in deformed profile, but not large enough to warrant further investigation.

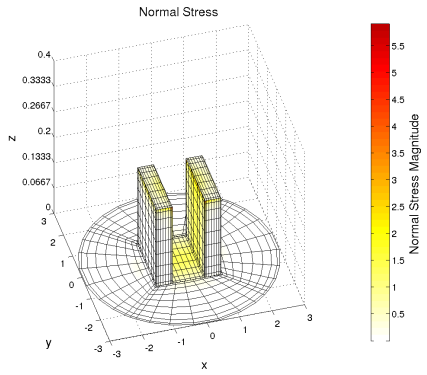

(a)

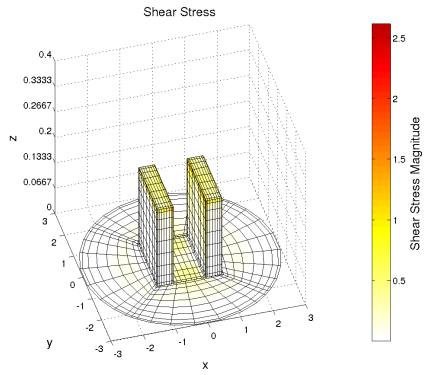

(b)

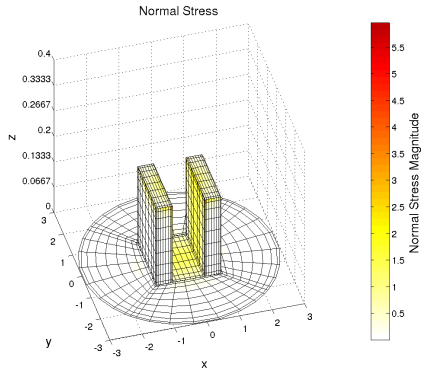

(c)

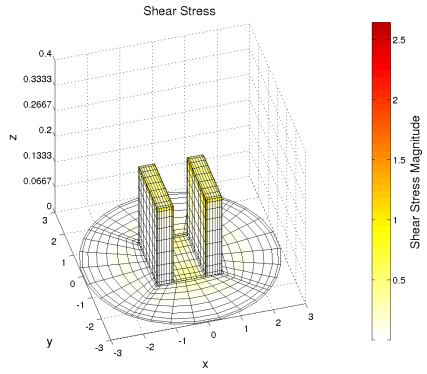

(d)

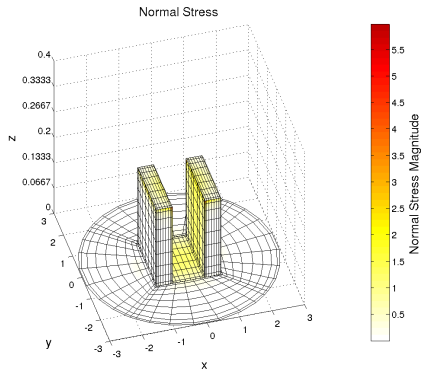

(e)

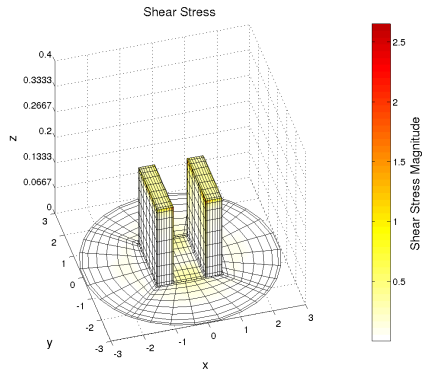

(f)

Figure 20. (a)-(b) Normal and shear stress distribution on the substrate for $B_d = 0.5$. (c)-(d) Normal and shear stress distribution on the substrate for $B_d = 1$. (e)-(f) Normal and shear stress distribution on the substrate for $B_d = 2$.

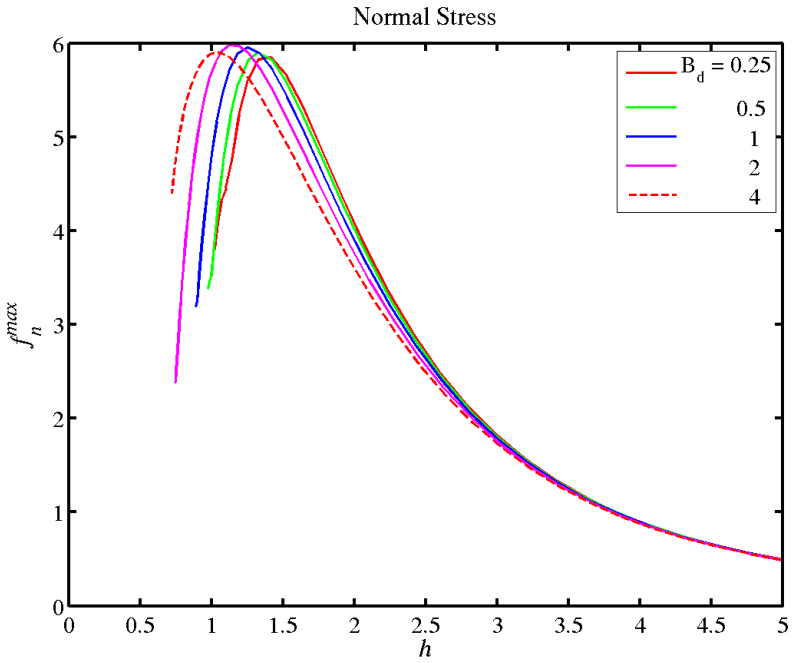

Figure 21. Maximum normal stress on the substrate as a function of height h and Bond number B_d.

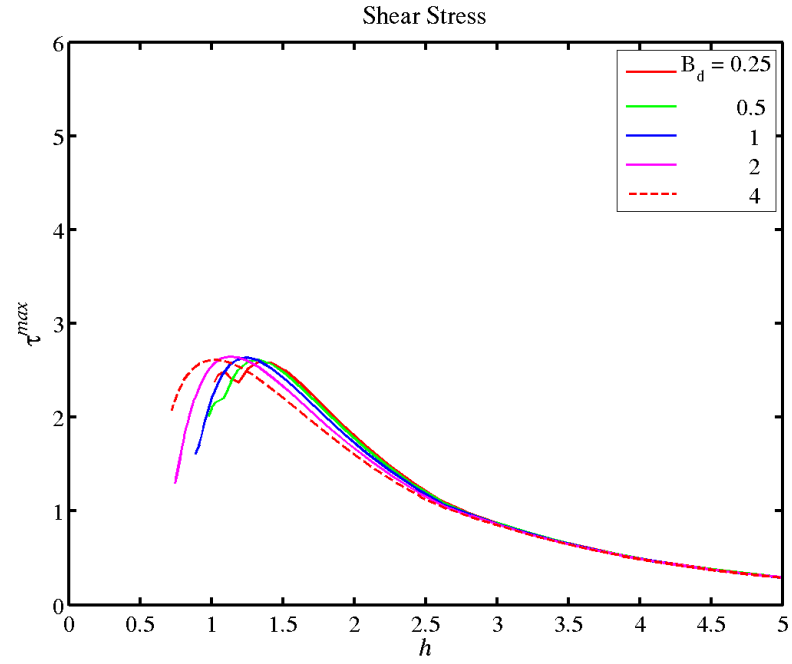

Figure 22. Maximum shear stress on the substrate as a function of height h and Bond number B_d.

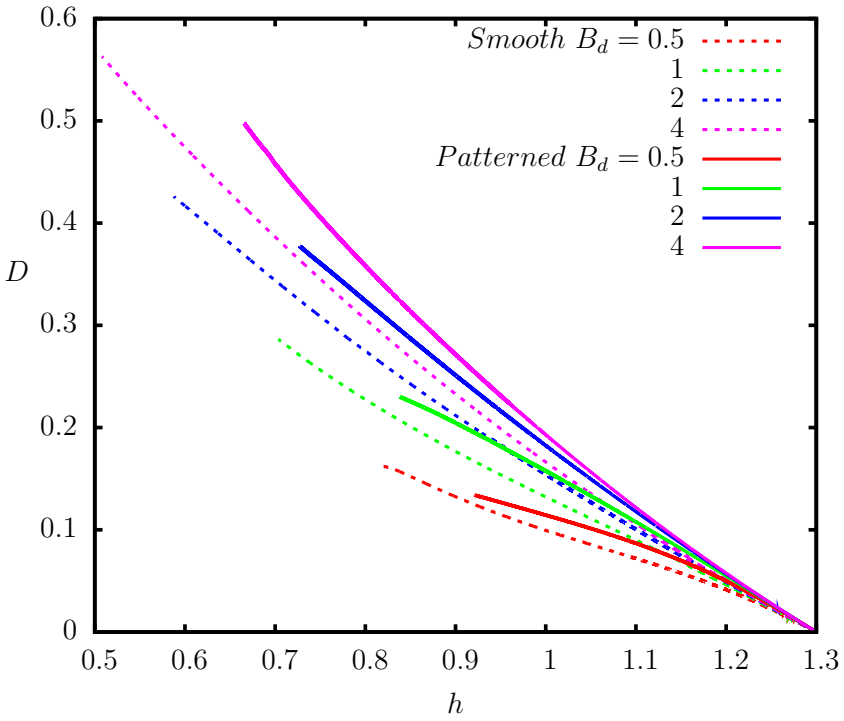

Figure 23. Droplet deformation D as a function of height h and Bond number B_d for $\lambda = 0.2$ and $h_0 = 1.3$.

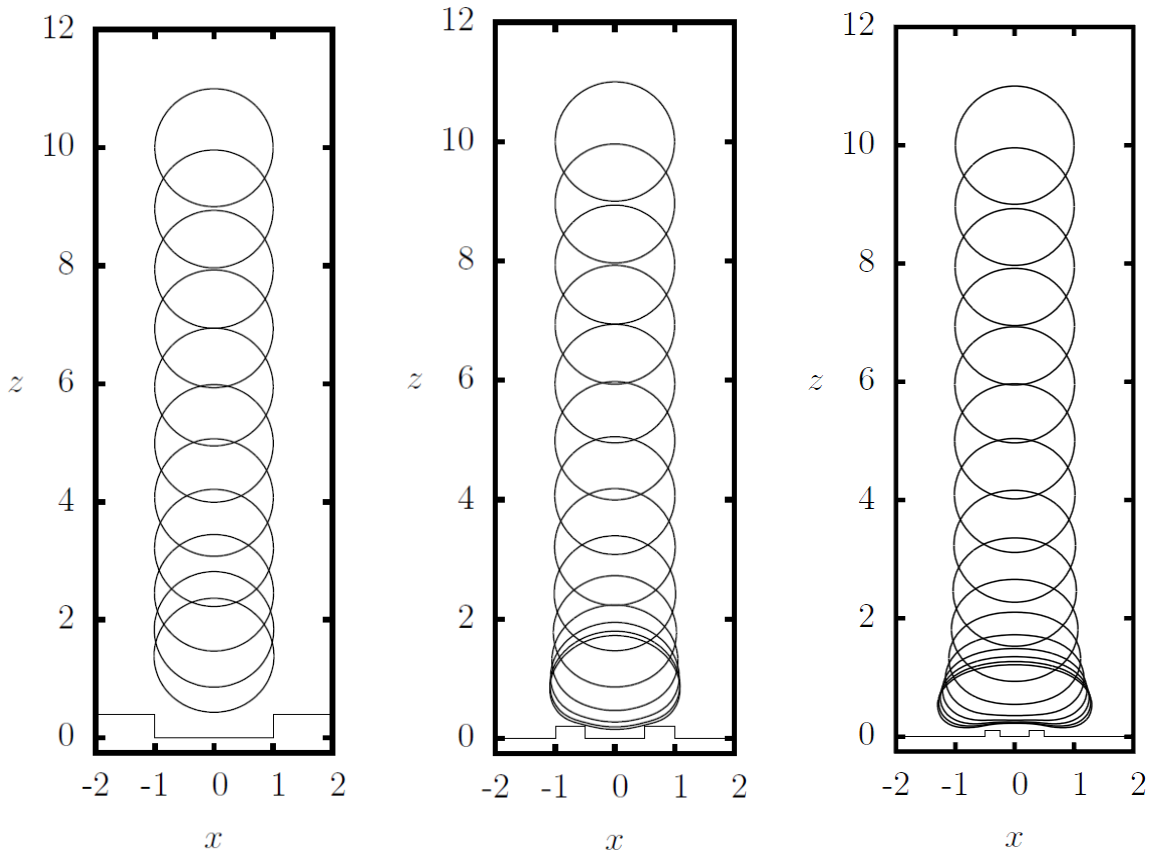

(a) (b) (c)

Figure 24. 2D droplet profiles for (a) case 1, (b) case 2, and (c) case 3. Cases 1, 2, and 3 represent a smaller droplet, the control size droplet, and a larger droplet, respectively. Case 1: $w_1 = 1$, $w_2 = 0.4$, $w_3 = 2$, $B_d = 0.25$. Case 2: $w_1 = 0.5$, $w_2 = 0.2$, $w_3 = 1$, $B_d = 1$. Case 3: $w_1 = 0.25$, $w_2 = 0.1$, $w_3 = 0.5$, $B_d = 4$.

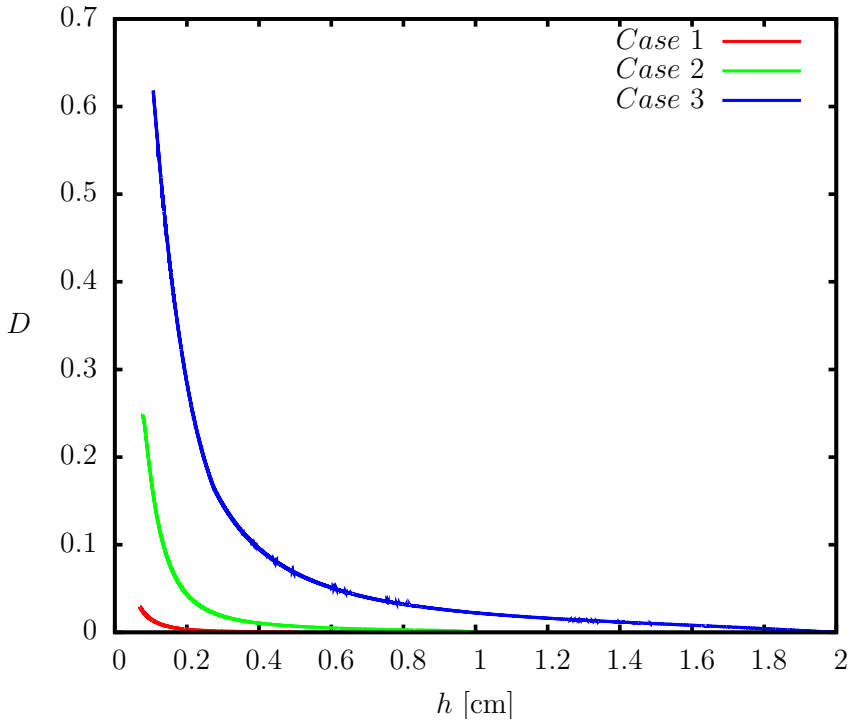

Figure 25. Droplet deformation D as a function of height h for $\lambda = 0.5$ and $h_0 = 10$. Parameters are listed in Fig. 24.

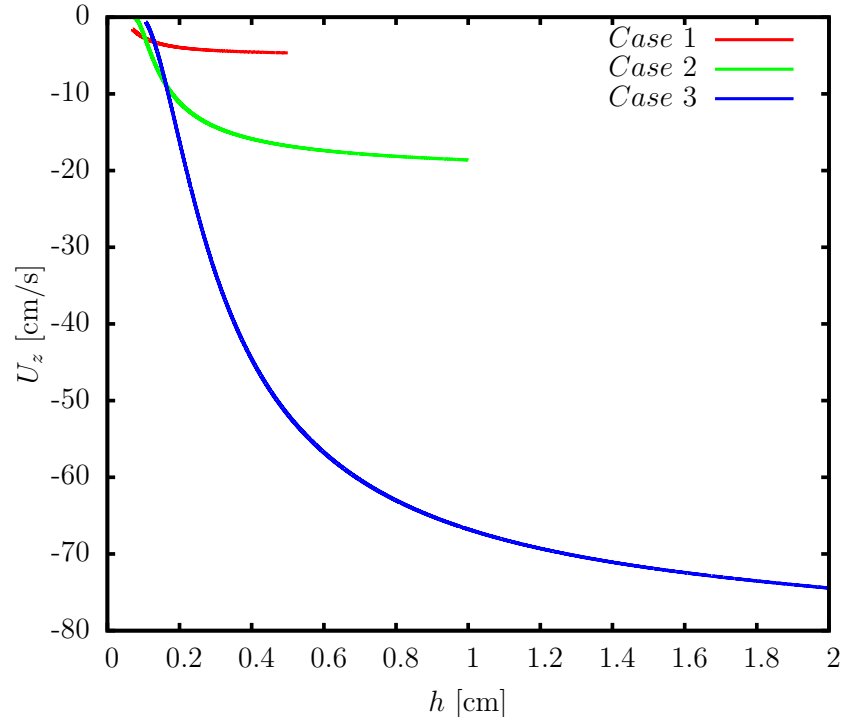

Figure 26. Droplet velocity U_z as a function of height h and droplet size. Parameters are listed in Fig. 24.

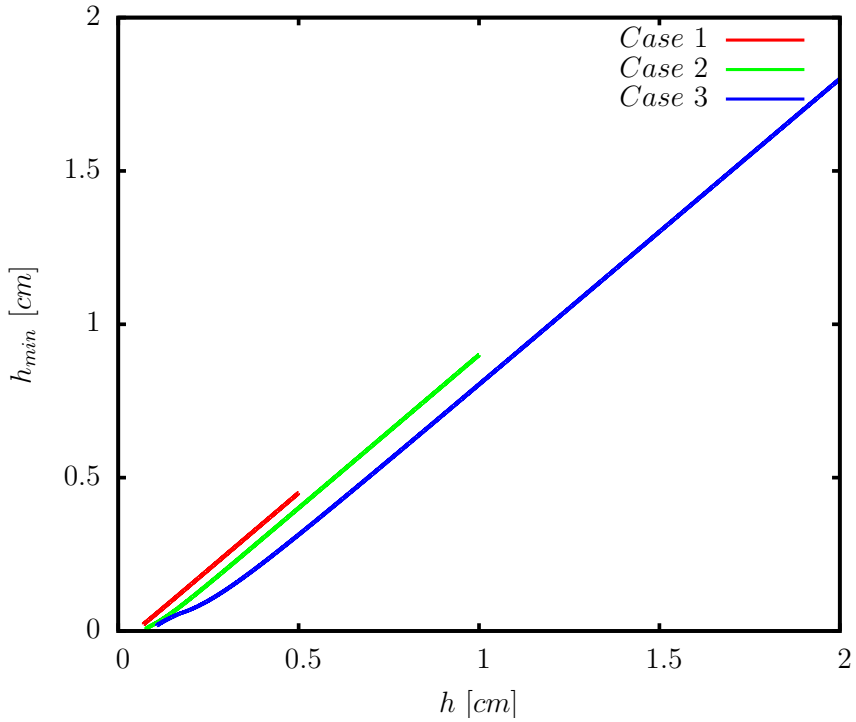

Figure 27. Minimum height h_{min} as a function of height h and droplet size. Parameters are listed in Fig. 24.

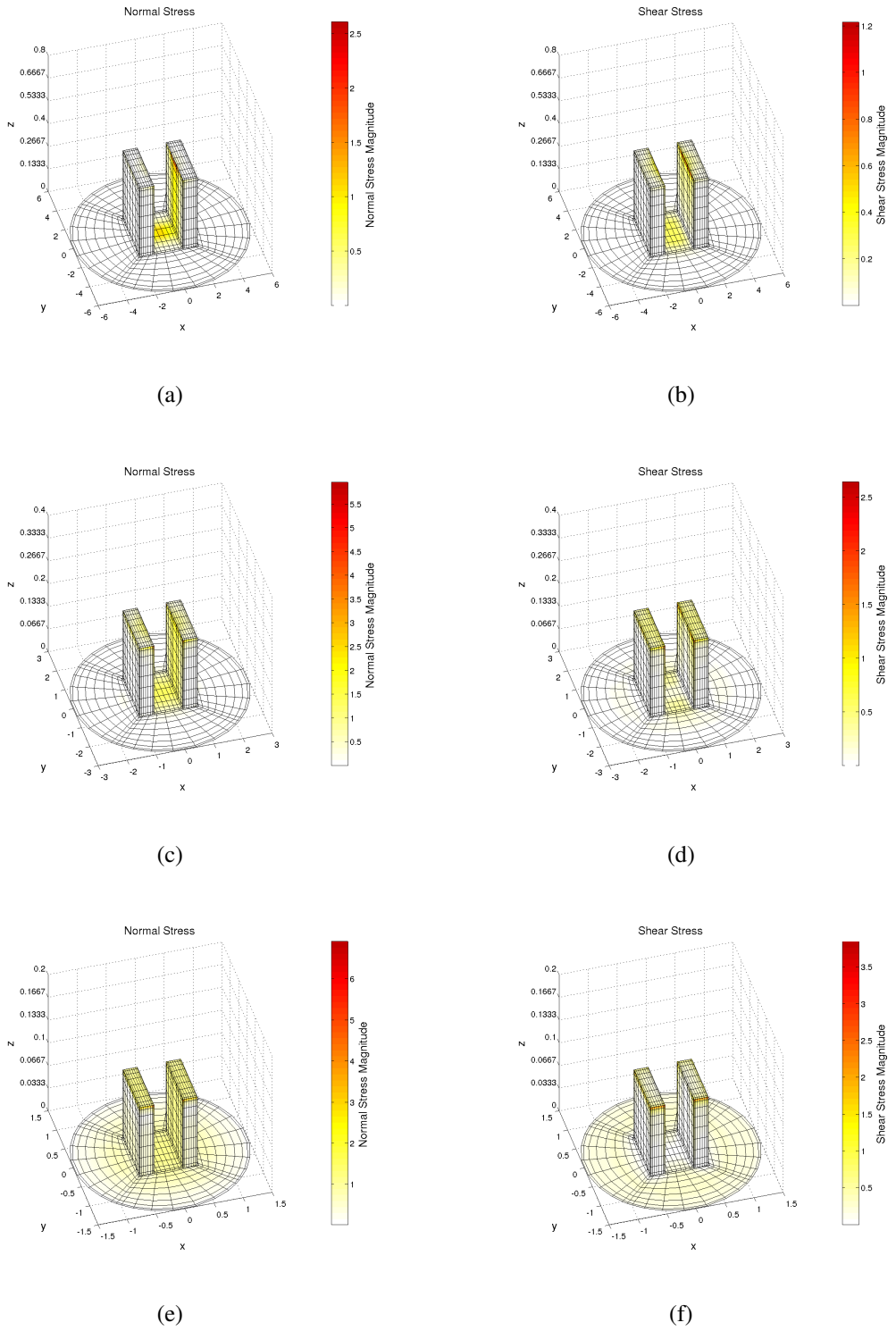

Figure 28. (a)-(b) Normal and shear stress distribution on the substrate for case 1, a small droplet. (c)-(d) Normal and shear stress distribution on the substrate for case 2. (e)-(f) Normal and shear stress distribution on the substrate for case 3, a large droplet. Parameters are listed in Fig. 24.

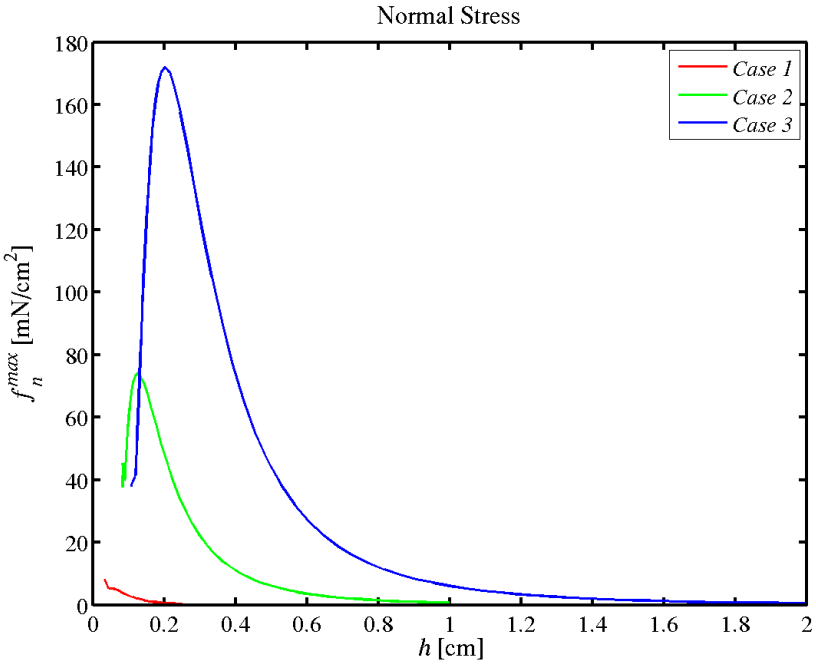

Figure 29. Maximum normal stress on the substrate as a function of height h and droplet size. Parameters are listed in Fig. 24.

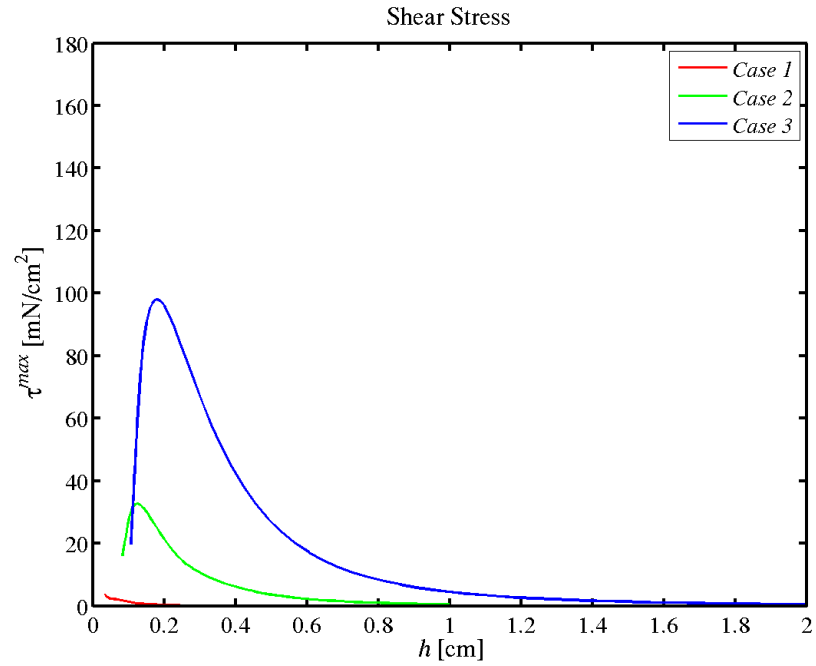

Figure 30. Maximum shear stress on the substrate as a function of height h and droplet size. Parameters are listed in Fig. 24.

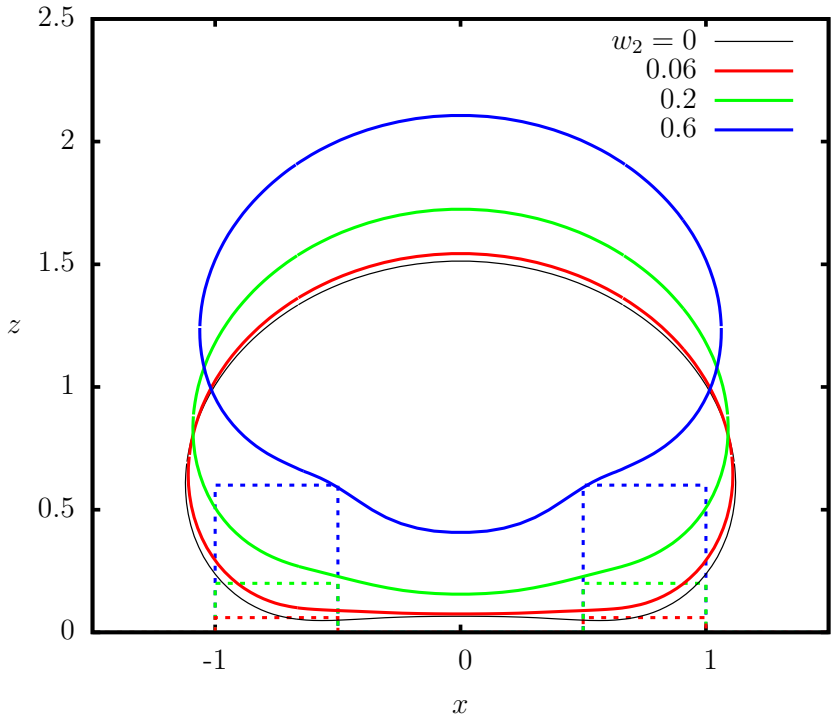

Figure 31. Droplet profiles for different pattern heights w_2 for $B_d = 1$, $\lambda = 0.5$, and $h_0 = 10$. For the patterned surface, $w_1 = 0.5$ and $w_3 = 1$.

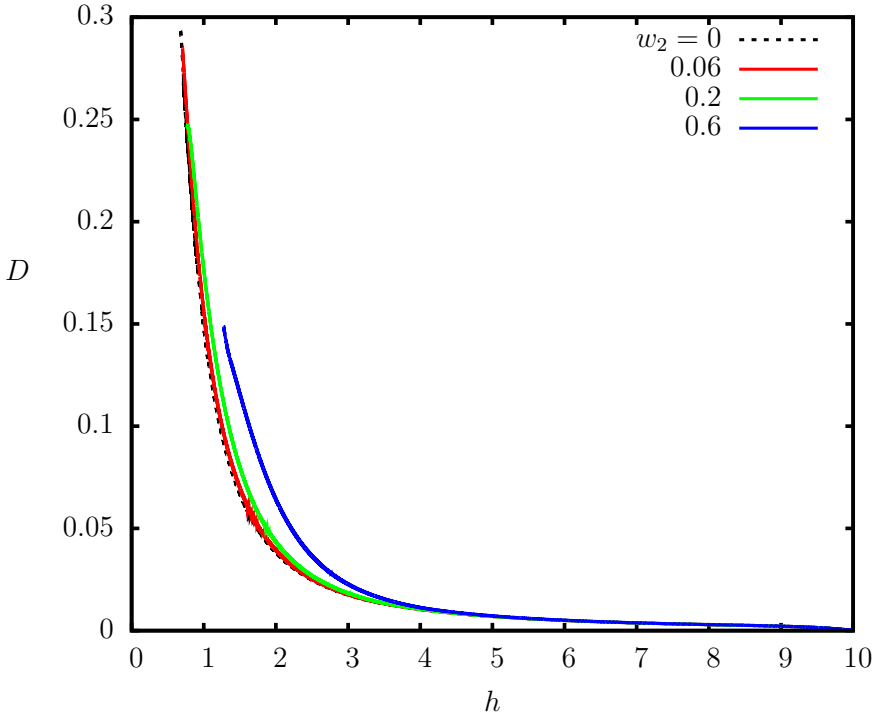

Figure 32. Droplet deformation D as a function of height h and pattern height w_2 for $B_d = 1$, $\lambda = 0.5$, and $h_0 = 10$. For the patterned surface, $w_1 = 0.5$ and $w_3 = 1$.

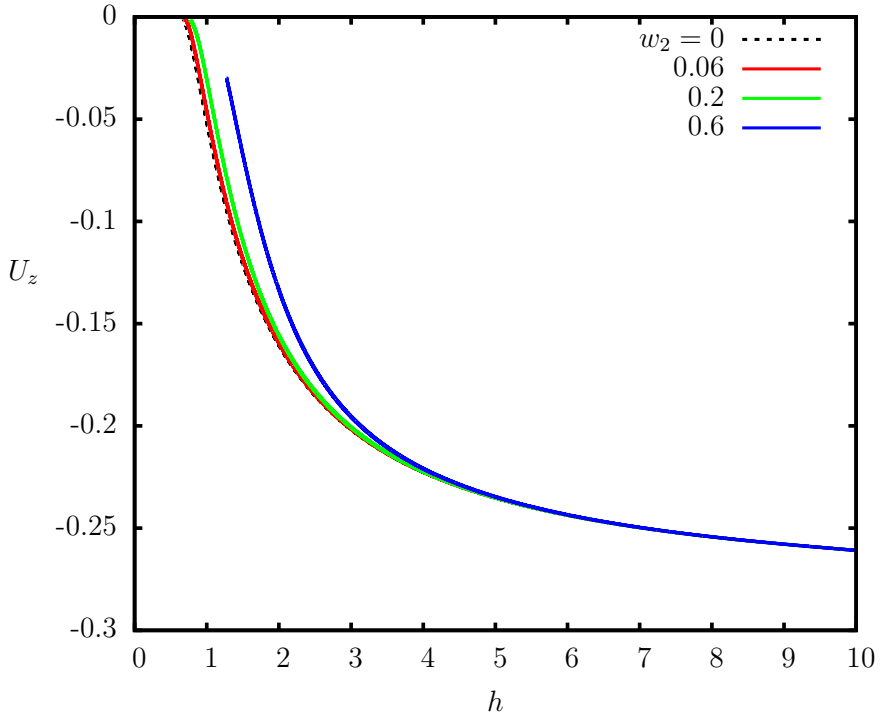

Figure 33. Droplet velocity U_z as a function of height h and pattern height w_2 for $B_d = 1$, $\lambda = 0.5$, and $h_0 = 10$. For the patterned surface, $w_1 = 0.5$ and $w_3 = 1$.

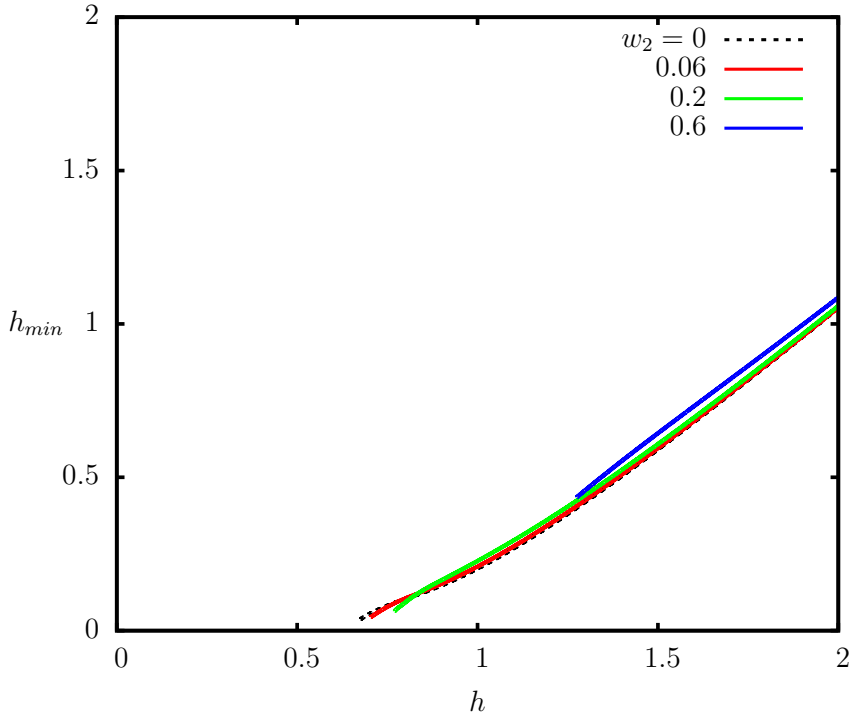

Figure 34. Minimum height h_{min} as a function of height h and pattern height w_2 for $B_d = 1$, $\lambda = 0.5$, and $h_0 = 10$. For the patterned surface, $w_1 = 0.5$ and $w_3 = 1$.

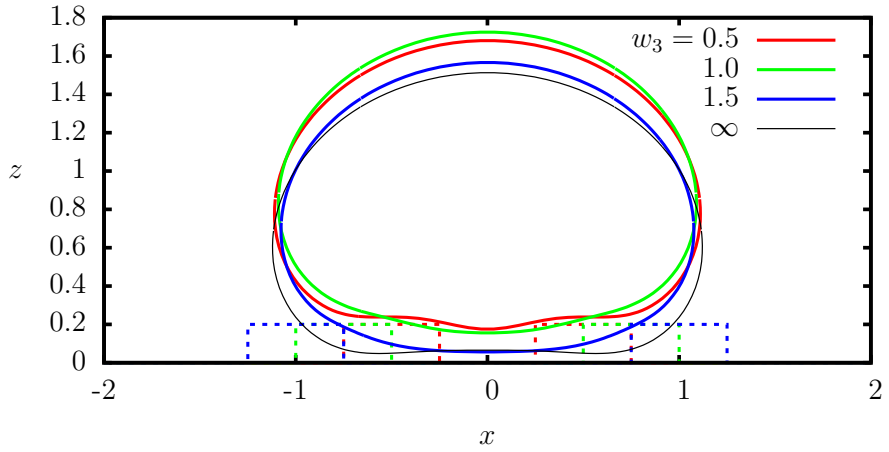

Figure 35. Droplet deformation D as a function of height h and pattern width w_3 for $B_d = 1$, $\lambda = 0.5$, and $h_0 = 10$. For the patterned surface, $w_1 = 0.5$ and $w_2 = 0.2$.

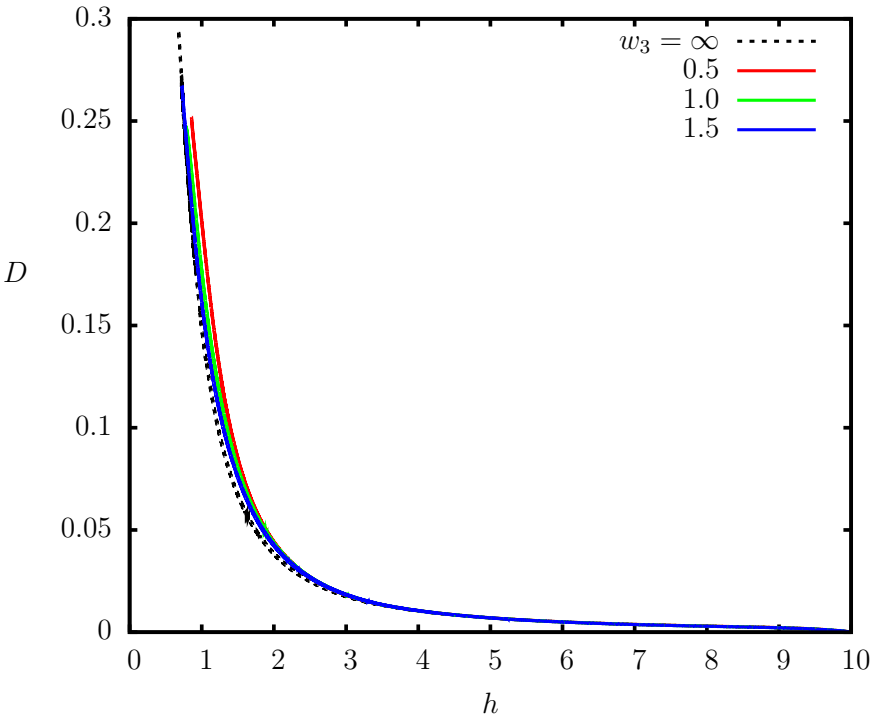

Figure 36. Droplet deformation D as a function of height h and pattern width w_3 for $B_d = 1$, $\lambda = 0.5$, and $h_0 = 10$. For the patterned surface, $w_1 = 0.5$ and $w_2 = 0.2$.

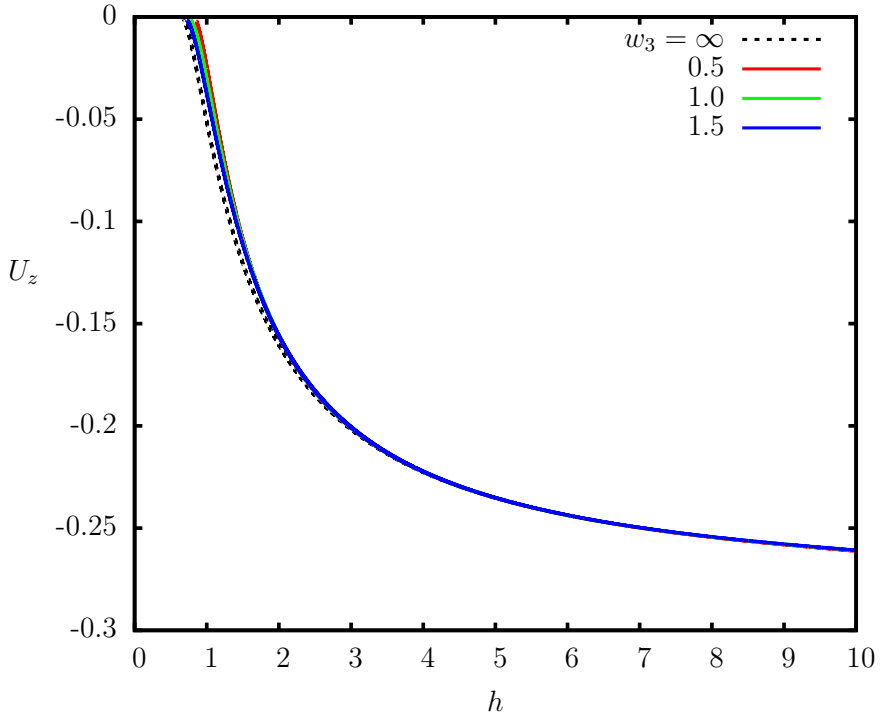

Figure 37. Droplet velocity U_z as a function of height h and pattern width w_3 for $B_d = 1$, $\lambda = 0.5$, and $h_0 = 10$. For the patterned surface, $w_1 = 0.5$ and $w_2 = 0.2$.

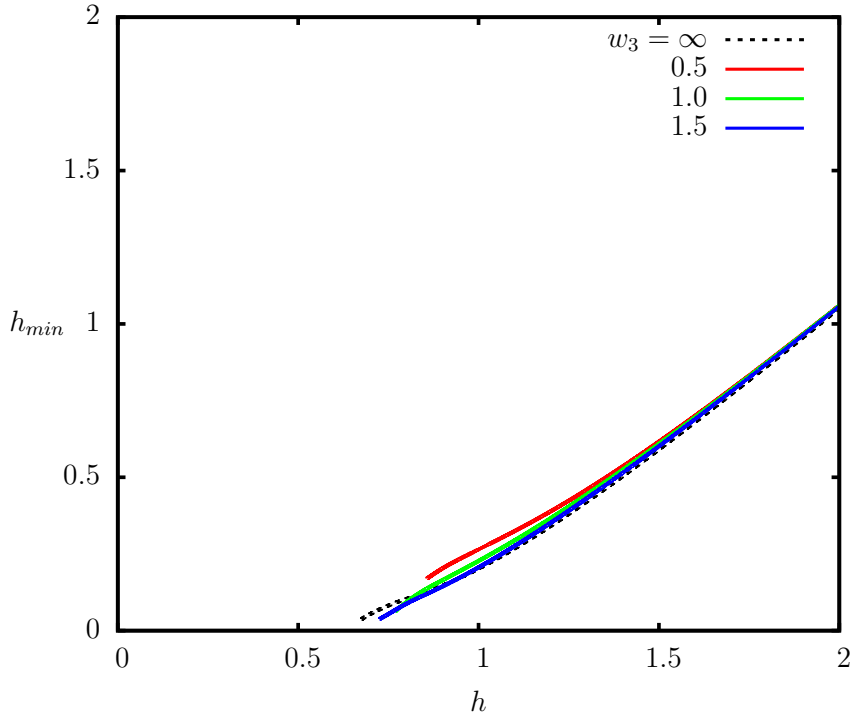

Figure 38. Minimum height h_{min} as a function of height h and pattern width w_3 for $B_d = 1$, $\lambda = 0.5$, and $h_0 = 10$. For the patterned surface, $w_1 = 0.5$ and $w_2 = 0.2$.

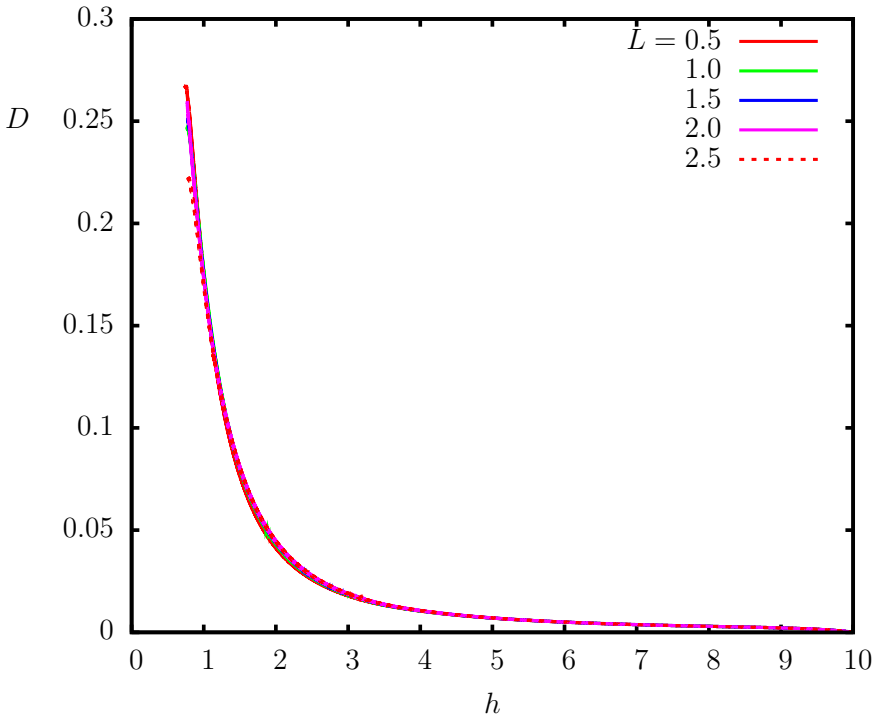

Figure 39. Droplet deformation D as a function of height h and pattern length L for $B_d = 1$, $\lambda = 0.5$, and $h_0 = 10$. For the patterned surface, $w_1 = 0.5$, $w_2 = 0.2$ and $w_3 = 1$.

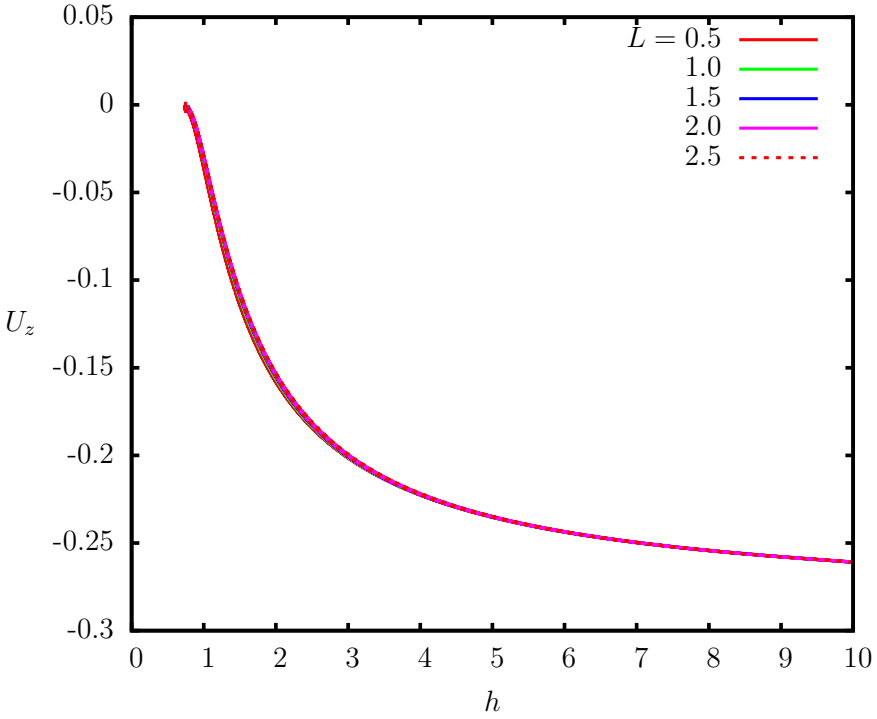

Figure 40. Droplet velocity U_z as a function of height h and pattern length L for $B_d = 1$, $\lambda = 0.5$, and $h_0 = 10$. For the patterned surface, $w_1 = 0.5$, $w_2 = 0.2$ and $w_3 = 1$.

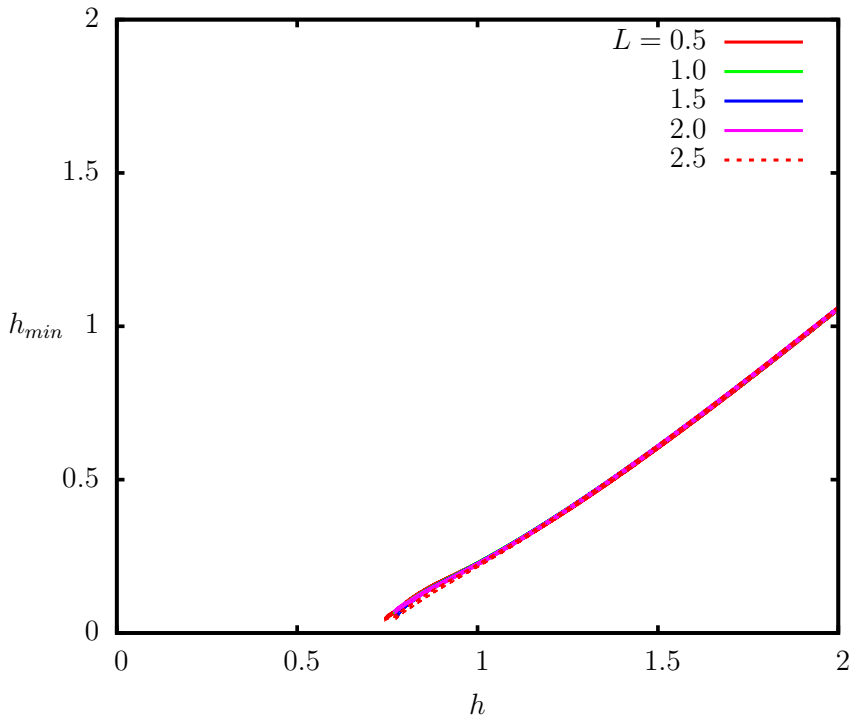

Figure 41. Minimum height h_{min} as a function of height h and pattern height w_2 for $B_d = 1$, $\lambda = 0.5$, and $h_0 = 10$. For the patterned surface, $w_1 = 0.5$, $w_2 = 0.2$ and $w_3 = 1$.

CHAPTER 5. DROPLET MOVING PARALLEL TO A PATTERNED SUBSTRATE

This section describes the results found for a droplet moving parallel to a wall with a patterned surface. Validation from section 4 was used to determine the appropriate time-step, mesh size, and substrate radius.

5.1. Results & discussion

The behavior of the droplet moving parallel to a patterned substrate is computed using the methods described. The droplet is at terminal velocity and moves across a single pattern on the substrate. The effect of B_d and pattern projection direction on the droplet dynamics is shown in the proceeding section.

In this preliminary study, simulations are presented for a droplet moving across a single pair of pillars with geometry identical to section 4. An example of this system is shown in Fig. 42 for both positive- and negative- projected patterns. We are currently working on simulating a droplet moving across an infinitely repeating pattern and determining the optimal discretization that reduces computational cost without sacrificing accuracy.

5.1.1. Influence of Bond number

The deformation of the droplet is computed as a function of x for different B_d and is shown in Fig. 43. The velocity of the droplet *away* from the substrate as a function of x is shown in Fig. 44. The distance x is parallel to the wall, in the direction of gravity, and across the pattern. The pattern is contained within $-1 \leq x \leq 1$ and the droplet initially begins at $x_0 = -4$. The droplet height h is measured between the droplet centroid and the substrate surface at $z = 0$.

It is clear that the overall deformation of the droplet increases as B_d is increased, consistent with previous observations. However, the deformation does not monotonically increasing to a steady value; it is instead perturbed by the pattern projecting out of the substrate which causes the droplet to deform more or less depending the location of the

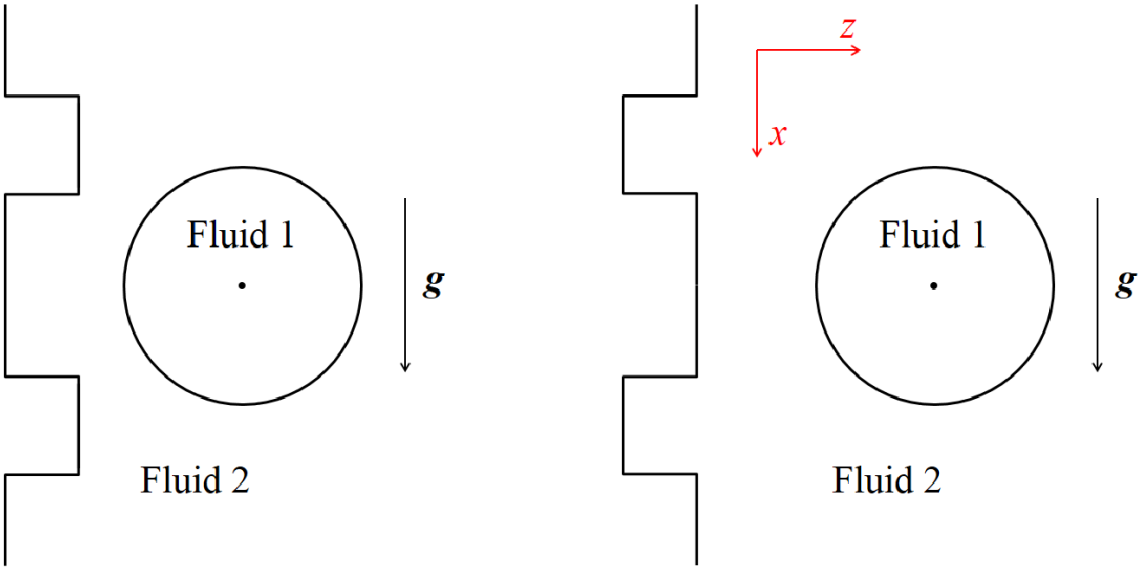

(a) (b)

Figure 42. Schematic for a droplet falling parallel to a patterned surface with (a) pattern projection *out of* the substrate, denoted as +P, and (b) pattern projection *into* the substrate, denoted as -P.

droplet. Interestingly, the most deformable droplet ($B_d = 3$) reaches its peak deformation directly above the second pillar while a moderately deformable droplet ($B_d = 1$) reaches its peak slightly before reaching the first pillar. All of the droplets trend towards a lower deformation after the pillars.

The velocity U_z away from the substrate also shows a waviness consistent with the presence of the pillars. Slightly before the first pillar, all of the droplets experience a large acceleration away from the substrate. This acceleration is then reversed when traversing between the two pillars. After the second pillar, the velocity of small B_d droplets actually becomes negative, and the droplet moves *towards* the substrate. For large enough B_d, the droplet will not move towards the substrate, but its velocity will become substantially lower after the second pillar. Wang *et al.* showed that for a smooth substrate, a droplet will monotonically move *away* from the substrate, never towards it [36].

The droplet trajectory h versus x is shown in Fig. 45. These trajectories follow the

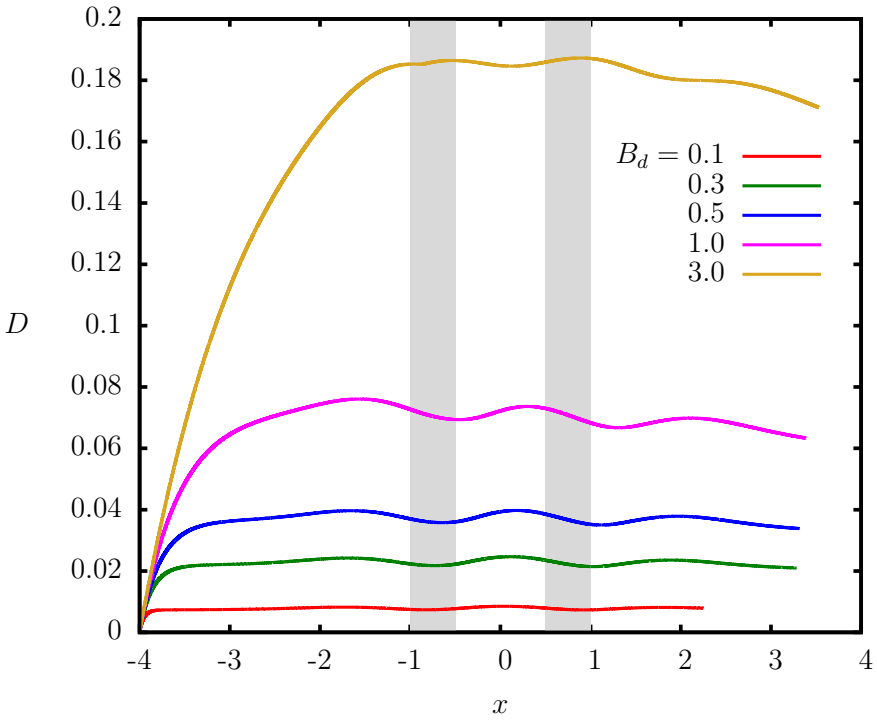

Figure 43. Droplet deformation D as a function of x and Bond number B_d for $\lambda = 1$ and $h_0 = 1.5$. The solid dark areas correspond to the location of the pattern. For the patterned surface, $w_1 = 0.5$, $w_2 = 0.2$ and $w_3 = 1$.

information obtained from the velocity plot: the droplet moves away from the substrate when it reaches the first pillar. For small B_d, the droplet will stabilize over the pattern and actually move towards the substrate after the second pillar. For large B_d, the droplet will continue moving away from the substrate.

5.1.2. Influence of pattern projection direction

For this study, we are interested in what happens with a pattern projecting *into* the substrate rather than *out of* the substrate like in the previous section 5.1.1. The two different pattern projection directions are shown in Fig. 42 with (a) the positive projection denoted as +P and (b) the negative projection denoted as -P.

The deformation of the droplet computed as a function of x for different B_d and projection direction is shown in Fig. 46. The velocity of the droplet *away* from the substrate as a function of x is shown in Fig. 47. The two cases, positive- and negative-projection,

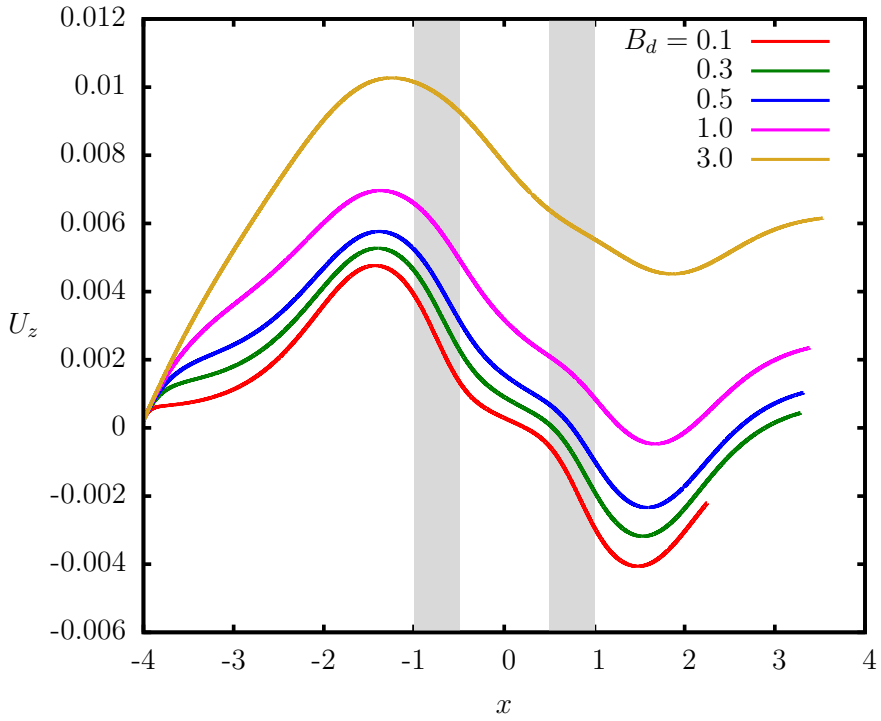

Figure 44. Droplet velocity U_z as a function of height h and B_d for $\lambda = 1$ and $h_0 = 1.5$. The solid dark areas correspond to the location of the pattern. For the patterned surface, $w_1 = 0.5$, $w_2 = 0.2$ and $w_3 = 1$.

follow the same general trend for deformation. However, the -P case does not have a large wavy trend like the +P case, it instead increases up to a peak value and slowly decreases past the pattern. The slight waviness in the -P case mirrors the waviness from the +P case: as the +P case deformation increases, the -P case deformation decreases slightly. The flat-plate case for $B_d = 0.3$ and 3 is depicted by the solid black lines in each figure and is consistent with Wang *et al.* [36]. The -P case closely matches the flat-plate case, while the +P case completely deviates from flat-plate as it passes the pillars. After passing the pattern, however, each simulation tends to approach the flat-plate solution, regardless of the pattern projection direction.

The velocity U_z follows a completely different trend for +P and -P cases as shown in Fig. 47. Again, the -P case mirrors the +P case: as the +P case accelerates away from the substrate, the -P case accelerates towards the substrate. However, the magnitude of the

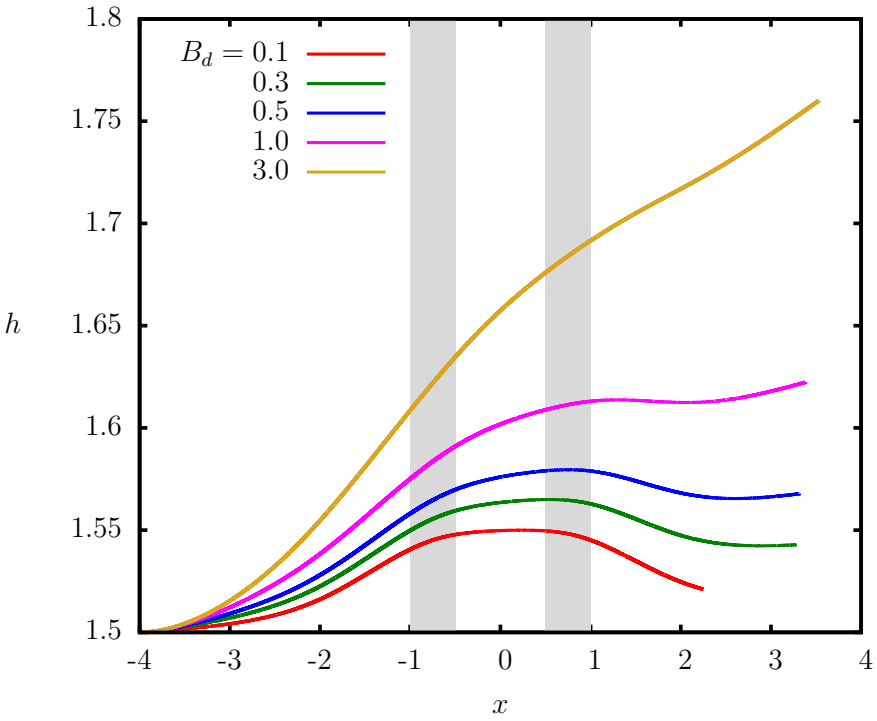

Figure 45. Centroid height h as a function of x and B_d for $\lambda = 1$ and $h_0 = 1.5$. The solid dark areas correspond to the location of the pattern. For the patterned surface, $w_1 = 0.5$, $w_2 = 0.2$ and $w_3 = 1$.

acceleration in the -P case is much smaller than the +P case. The -P case almost never has a negative velocity, only very slightly for the lowest B_d droplet. Compared with the flat-plate solution, the -P case very closely matches for high B_d and deviates slightly for low B_d. The +P case completely deviates from the flat-plate regardless of B_d. Again, each simulation tends to approach the flat-plate solution after passing the pattern.

The droplet trajectory h versus x is shown in Fig. 48 for both +P and -P cases. When moving across the pattern, the droplets in the +P case move away from the substrate, while the droplets in the -P case move across the pattern with little effect.

The most surprising result from this study is that both the +P and -P cases approach the flat-plate solution after the pattern. This is an extremely intriguing result: the pattern projection direction does not seem to have much effect on the droplet's final position. At this low-*Re*flow, any motion caused by the pillars is negated by an equal and opposite

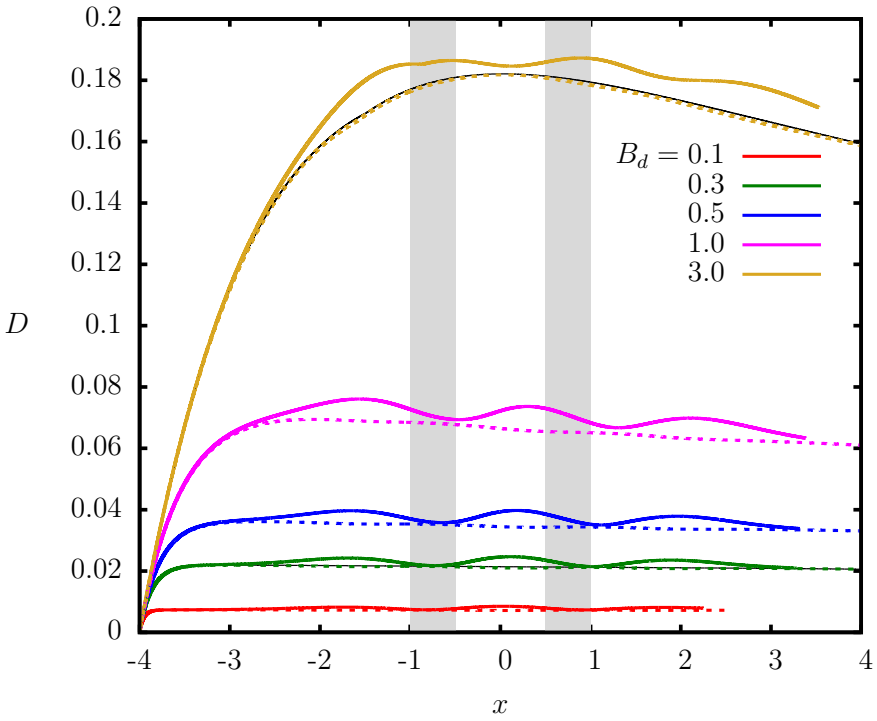

Figure 46. Droplet deformation D as a function of x and B_d for $\lambda = 1$ and $h_0 = 1.5$. Solid lines are for a positive-projected pattern (out of the substrate) while dashed lines are for a negative-projected pattern (into the substrate). Solid black lines represent solutions for a flat substrate at $B_d = 0.3$ and 3. The solid dark areas correspond to the location of the pattern. For the patterned surface, $w_1 = 0.5$, $w_2 = 0.2$ and $w_3 = 1$.

motion after passing the pillars. It is possible that this result can be extrapolated to various other obstacles such as cylindrical humps or other geometries. This may be a topic for more study.

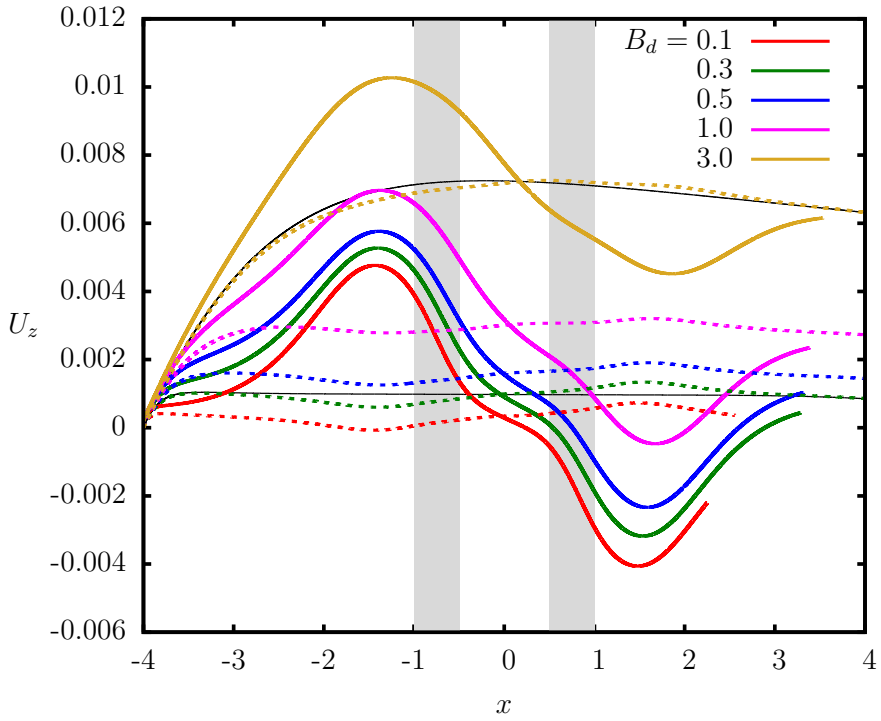

Figure 47. Droplet velocity U_z as a function of x and B_d for $\lambda = 1$ and $h_0 = 1.5$. Solid lines are for a positive-projected pattern (out of the substrate) while dashed lines are for a negative-projected pattern (into the substrate). Solid black lines represent solutions for a flat substrate at $B_d = 0.3$ and 3. The solid dark areas correspond to the location of the pattern. For the patterned surface, $w_1 = 0.5$, $w_2 = 0.2$ and $w_3 = 1$.

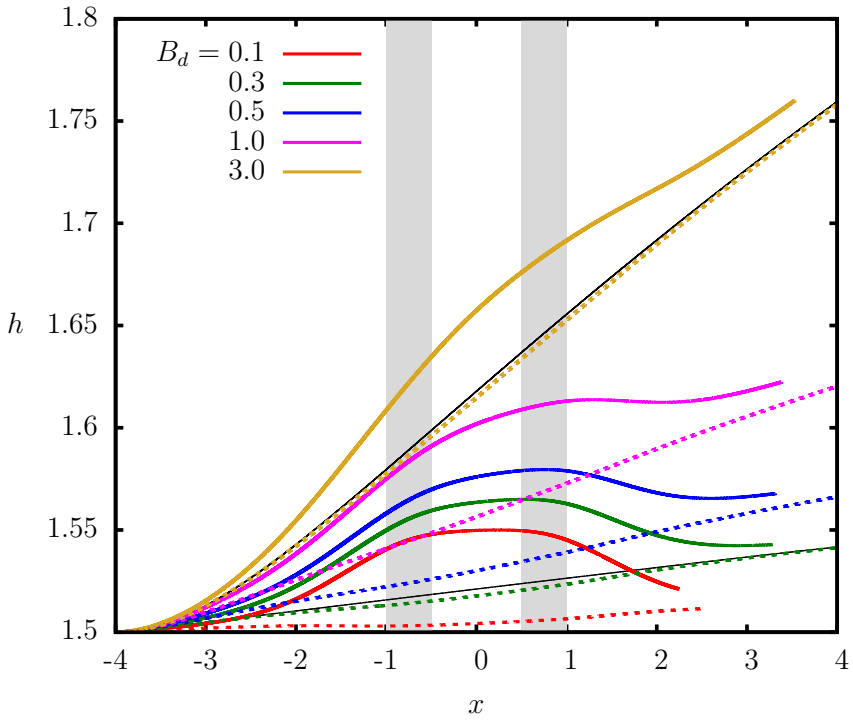

Figure 48. Centroid height h as a function of x and B_d. Solid lines are for a positive-projected pattern (out of the substrate) while dashed lines are for a negative-projected pattern (into the substrate). Solid black lines represent solutions for a flat substrate at $B_d = 0.3$ and 3. The solid dark areas correspond to the location of the pattern. For the patterned surface, $w_1 = 0.5$, $w_2 = 0.2$ and $w_3 = 1$.

CHAPTER 6. CONCLUSIONS

In this study, a 3D spectral boundary element method has been employed to analyze droplet dynamics moving towards a patterned substrate under the influence of gravity. Two problems were investigated: a droplet perpendicularly approaching a patterned surface and a droplet moving parallel across a patterned surface. For a droplet approaching perpendicularly, the influences of B_d, droplet size, and pattern parameters on the droplet behavior were investigated. It has been shown that a micropattern on a substrate can indeed be used to control the deformation and behavior of a droplet moving either perpendicularly towards the pattern or parallel across it.

A larger B_d results in increased deformation while the vertical velocity remains largely unaffected. Increased B_d also causes the droplet to flatten and hover above the substrate rather than contact it. Additionally, for more deformable droplets the peak stress occurs when the droplet centroid is closer to the substrate. The stress distribution over the substrate is mostly unaffected by B_d.

Droplet size is also shown to have a large effect on the droplet and substrate. Larger droplets result in greatly increased deformation and velocity. Small droplets simply fall between the pillars and remain spherical while large droplets spread out across the entire pattern. The stress magnitude is much larger for large droplets and is distributed over the entire pattern while small droplets produce much lower stress concentrated directly under the droplet.

The different pattern parameters studied also had a profound impact on the way droplets interact with the surface. The existence of a pattern causes the droplet to protrude out between the pillars rather than dimple as it does on a flat surface. Increasing the height of the pillars increases this protrusion and, in turn, the deformation D. Increasing the gap between the pillars also affects this: small gaps cause the droplet to protrude between the pillars, while flat-plate behavior is observed for very large gaps between pillars. Lastly,

the pattern length has very little effect on the droplet as long as it is on the same order of magnitude as the droplet radius.

For a droplet moving parallel to the patterned substrate, the Bond number was investigated as well as the projection direction of the pattern. An increased B_d yields higher deformation, but causes peak deformation to occur at different places. The velocity away from the substrate is also increased, and low B_d droplets will sometimes move towards the substrate, while high B_d droplets will always move away. It also seems that large B_d droplets are much less affected by the pillars and more closely follow flat-plate results.

The projection direction into or out of the substrate show that patterns projected out of the substrate result in higher deformation. The velocity away from the substrate follows a completely different pattern for positive and negative projections, with positive projections showing much larger velocity magnitudes. However, for both cases, the droplet eventually migrates near the same location after the pattern, which may be true for other obstacles as well.

CHAPTER 7. FUTURE WORK

We are currently working on implementing the symmetry boundary condition into the method so that an infinitely repeating pattern can be simulated. This may also allow us to more accurately model an infinite substrate without large numbers of elements, reducing the computational cost.

This research included studies done on droplets moving perpendicular and parallel to the substrate, but we are also working on droplets approaching at angles to the patterned substrate. Simulations have been performed for droplets approaching flat substrates at an incline [25], but never for patterned surfaces.

We are also exploring the use of different patterns on the substrate, including square pillars repeated in two directions, cylindrical pillars, and serrated triangular pillars. Each pattern may have a unique interaction with the droplet, allowing us to better understand and control the droplet dynamics.

REFERENCES

[1] H. Andersson and A. Van den Berg, *Microfluidic devices for cellomics: a review*, Sensors and Actuators B: Chemical **92** (2003), no. 3, 315–325.

[2] E. Ascoli, D. Dandy, and L. Leal, *Buoyancy-driven motion of a deformable drop toward a planar wall at low reynolds number*, J. Fluid Mech. **213** (1990), 287–311.

[3] D. S. Dandy and L. G. Leal, *Buoyancy-driven motion of a deformable drop through a quiescent liquid at intermediate reynolds numbers*, Journal of Fluid Mechanics **208** (1989), 161–192.

[4] P. Dimitrakopoulos and J. Higdon, *Displacement of fluid droplets from solid surfaces in low-reynolds-number shear flows*, Journal of Fluid Mechanics **336** (1997), 351–378.

[5] P. Dimitrakopoulos and J. Higdon, *On the displacement of three-dimensional fluid droplets from solid surfaces in low-reynolds-number shear flows*, Journal of Fluid Mechanics **377** (1998), 189–222.

[6] P. Dimitrakopoulos and J. Higdon, *On the gravitational displacement of three-dimensional fluid droplets from inclined solid surfaces*, Journal of Fluid Mechanics **395** (1999), 181–209.

[7] P. Dimitrakopoulos and J. Higdon, *On the displacement of three-dimensional fluid droplets adhering to a plane wall in viscous pressure-driven flows*, Journal of Fluid Mechanics **435** (2001), 327–350.

[8] P. Dimitrakopoulos and J. Higdon, *On the displacement of fluid bridges from solid surfaces in viscous pressure-driven flows*, Physics of Fluids (1994-present) **15** (2003), no. 10, 3255–3258.

[9] P. Dimitrakopoulos, *Computational studies of droplet displacement in stokes flow*, Master's thesis, University of Illinois, 1996.

[10] P. Dimitrakopoulos, *Interfacial dynamics in stokes flow via a three-dimensional fully-implicit interfacial spectral boundary element algorithm*, Journal of Computational Physics **225** (2007), no. 1, 408–426.

[11] J. Q. Feng, *A deformable liquid drop falling through a quiescent gas at terminal velocity*, J. Fluid Mech. **658** (2010), 438–462.

[12] M. Goto, T. Tsukahara, K. Sato, and T. Kitamori, *Micro-and nanometer-scale patterned surface in a microchannel for cell culture in microfluidic devices*, Analytical and bioanalytical chemistry **390** (2008), no. 3, 817–823.

[13] J. Higdon and G. Muldowney, *Resistance functions for spherical particles, drops and bubbles in cylindrical tubes*, J. Fluid Mech. **298** (1995), 193–204.

[14] R. Kannan and D. Sivakumar, *Drop impact process on a hydrophobic grooved surface*, Colloid Surface A **317** (2008), 694–704.

[15] E. Klaseboer, J.-P. Chevaillier, A. Maté, O. Masbernat, and C. Gourdon, *Model and experiments of a drop impinging on an immersed wall*, Physics of Fluids (1994-present) **13** (2001), no. 1, 45–57.

[16] D. Legendre, C. Daniel, and P. Guiraud, *Experimental study of a drop bouncing on a wall in a liquid*, Physics of Fluids **17** (2005), 097105.

[17] D. Legendre, R. Zenit, C. Daniel, and P. Guiraud, *A note on the modelling of the bouncing of spherical drops or solid spheres on a wall in viscous fluid*, Chemical engineering science **61** (2006), no. 11, 3543–3549.

[18] D. R. Link, E. Grasland-Mongrain, A. Duri, F. Sarrazin, Z. Cheng, G. Cristobal, M. Marquez, and D. A. Weitz, *Electric control of droplets in microfluidic devices*, Angewandte Chemie International Edition **45** (2006), no. 16, 2556–2560.

[19] J. Magnaudet, S. Takagi, and D. Legendre, *Drag, deformation and lateral migration of a buoyant drop moving near a wall*, Journal of Fluid Mechanics **476** (2003), 115–157.

[20] J. Moláček and J. W. Bush, *A quasi-static model of drop impact*, Phys. Fluids **24** (2012), 127103.

[21] G. Muldowney and J. Higdon, *A spectral boundary element approach to three-dimensional stokes flow*, Journal of Fluid Mechanics **298** (1995), 167–192.

[22] M.-J. Ni, S. Komori, and N. B. Morley, *Direct simulation of falling droplet in a closed channel*, Int. J. Heat Mass Tran. **49** (2006), 366–376.

[23] M. Pasandideh-Fard, S. Chandra, and J. Mostaghimi, *A three-dimensional model of droplet impact and solidification*, International Journal of Heat and Mass Transfer **45** (2002), no. 11, 2229–2242.

[24] C. Pozrikidis, *Boundary integral and singularity methods for linearized viscous flow*, Cambridge University Press, New York, NY, 1992.

[25] S. Quan, *Dynamics and thin film drainage of a deformable droplet moving towards a solid wall with finite inertia*, RSC Advances **2** (2012), no. 5, 1927–1935.

[26] N. C. Reis Jr, R. F. Griffiths, and J. M. Santos, *Numerical simulation of the impact of liquid droplets on porous surfaces*, Journal of Computational Physics **198** (2004), no. 2, 747–770.

[27] S. S. Sadhal, P. S. Ayyaswamy, and J. N.-C. Chung, *Transport phenomena with drops and bubbles*, vol. 18, Springer New York, 1997.

[28] D. Sivakumar, K. Katagiri, T. Sato, and H. Nishiyama, *Spreading behavior of an impacting drop on a structured rough surface*, Phys. Fluids **17** (2005), 100608.

[29] J. P. Smith, A. C. Barbati, S. M. Santana, J. P. Gleghorn, and B. J. Kirby, *Microfluidic transport in microdevices for rare cell capture*, Electrophoresis **33** (2012), no. 21, 3133–3142.

[30] H. A. Stone, A. D. Stroock, and A. Ajdari, *Engineering flows in small devices: microfluidics toward a lab-on-a-chip*, Annu. Rev. Fluid Mech. **36** (2004), 381–411.

[31] F. Takemura, S. Takagi, J. Magnaudet, and Y. Matsumoto, *Drag and lift forces on a bubble rising near a vertical wall in a viscous liquid*, Journal of Fluid Mechanics **461** (2002), 277–300.

[32] G. I. Taylor, *The viscosity of a fluid containing small drops of another fluid*, Proceedings of the Royal Society of London. Series A **138** (1932), no. 834, 41–48.

[33] G. Taylor, *The formation of emulsions in definable fields of flow*, Proceedings of the Royal Society of London. Series A **146** (1934), no. 858, 501–523.

[34] T. Taylor and A. Acrivos, *On the deformation and drag of a falling viscous drop at low reynolds number*, Journal of Fluid Mechanics **18** (1964), no. 03, 466–476.

[35] V. Vaikuntanathan and D. Sivakumar, *Directional motion of impacting drops on dual-textured surfaces*, Phys. Rev. E **86** (2012), 036315.

[36] Y. Wang and P. Dimitrakopoulos, *A three-dimensional spectral boundary element algorithm for interfacial dynamics in Stokes flow*, Phys. Fluids **18** (2006), 082106.

[37] Y. Wang, *Numerical studies of stokes flow in confined geometries*, Master's thesis, University of Maryland-College Park, 2004.

[38] A. R. Wheeler, W. R. Throndset, R. J. Whelan, A. M. Leach, R. N. Zare, Y. H. Liao, K. Farrell, I. D. Manger, and A. Daridon, *Microfluidic device for single-cell analysis*, Analytical chemistry **75** (2003), no. 14, 3581–3586.

[39] Y. Yao, Y. Wang, and K. M. Beussman, *Deformation and migration of a leaky-dielectric droplet in a steady non-uniform electric field*, Microfluidics and Nanofluidics (2014), 1–15.

[40] S. G. Yiantsios and R. H. Davis, *On the buoyancy-driven motion of a drop towards a rigid surface or a deformable interface*, J. Fluid Mech. **217** (1990), 547–573.

[41] G. Zhu, A. Mammoli, and H. Power, *A 3-d indirect boundary element method for bounded creeping flow of drops*, Engineering analysis with boundary elements **30** (2006), no. 10, 856–868.

[42] A. Z. Zinchenko, M. A. Rother, and R. H. Davis, *A novel boundary-integral algorithm for viscous interaction of deformable drops*, Physics of Fluids (1994-present) **9** (1997), no. 6, 1493–1511.